Physicochem. Probl. Miner. Process., 62(4), 2026, 226426

http://www.journalssystem.com/ppmp

Physicochemical Problems of Mineral Processing

ISSN 1643-1049

Empirical drag coefficient correlation for uncoated and oil-coated bubbles: experimental development and multi-dataset validation

Diego Poblete [1], Claudio Acuña [2], Claudio Leiva [3]

[1] Oulu Mining School, University of Oulu, 90570, Oulu, Finland

[2] Departamento de Ingeniería Química y Ambiental, Universidad Técnica Federico Santa María, 2390123, Valparaíso, Chile

[3] Departamento de Ingeniería Química y de Medio Ambiente Universidad Católica del Norte, 1270709, Antofagasta, Chile

Corresponding author: diego.poblete@oulu.fi (Diego Poblete)

Abstract: Coated bubbles arise in flotation columns and solvent extraction contactors; however, no unified correlation predicts their drag coefficient from dimensionless parameters across multiple fluid systems. This work develops an empirical power-law correlation from 2,268 observations spanning three continuous phases (water, 26 wt% NaCl, 30 wt% sucrose) and two organic phases (kerosene and sunflower oil), covering viscosity ratios from 0.34 to 58 and Reynolds numbers from 56 to 894. Drag modification by oil coating depends critically on the viscosity ratio: coated bubbles exhibit higher drag than uncoated bubbles in water and salt systems but lower drag in the sucrose system, where the coating is less viscous than the continuous phase. Three power-law correlations were developed: an uncoated bubble model (Mean Absolute Percentage Error (MAPE) = 1.2%), a coated-bubble model (MAPE = 6.9%), and a unified model (MAPE = 2%) that reduces to the uncoated bubble model when no coating is present. The Reynolds and Eötvös numbers are the dominant parameters; Morton number, coating fraction, and viscosity ratio are secondary within the tested parameter window ($0.34 \leq \eta \leq 58$). Validation against 25 independent external datasets (2,882 uncoated bubble and 28 coated-bubble measurements, 2,910 total) yielded a mean $R^2 = 0.97$ and a MAPE of 5–6% for the uncoated bubble subset; coated-bubble external validation, while consistent with model predictions, is based on a limited number of data points and should be interpreted as preliminary. The model is valid for $30 < Re < 1000$ and $0.1 < Eo < 10$, providing empirical drag closure for drift-flux and multiphase flow models applied to single-bubble systems under quiescent conditions within this parameter window.

Keywords: coated bubble, drag coefficient, empirical equation, oily bubble

1. Introduction

Bubble hydrodynamics presents a complex problem: even a single bubble rising in a quiescent liquid exhibits trajectory instabilities that transition from rectilinear to zigzag and helical paths as bubble size increases, a phenomenon known as Leonardo's paradox that was recently explained through high-resolution numerical simulations (Herrada & Eggers, 2023). This complexity is not merely of academic interest, as the same interfacial and inertial forces that govern path instability also control terminal velocity and drag, which determines bubble behavior in industrial processes.

Bubbles are central to a wide range of engineering processes in which the gas-liquid interface governs mass transfer, reaction kinetics, and separation efficiency. In bubble column reactors, a dispersed gaseous phase interacts with a continuous liquid phase to promote chemical reactions and gas absorption (Besagni et al., 2018). In mineral flotation, bubble-particle attachment underpins the selective separation of hydrophobic minerals from gangue (Ayoglu et al., 2025). In CO_2 absorption columns, bubbles control

DOI: 10.37190/ppmp/226426

interfacial mass transfer rates, while in solvent extraction systems, they determine contact time and extraction kinetics. Among these, terminal velocity sets the bubble residence time, controls gas holdup, and determines the interfacial area available for mass transfer. The terminal velocity cannot be predicted from density differences and geometry alone; it is coupled to the drag coefficient, which serves as the controlling variable through which fluid properties, flow regime, and interfacial characteristics enter the force balance.

In bubble column reactors, the drift-flux methodology provides a framework for relating gas holdup to bubble rise velocity and, through it, to mean bubble size (Masliyah, 1979; Wallis, 1969; Yianatos et al., 1988). The accuracy of this approach depends on the drag correlation used, as any error in the model is propagated into the bubble-size prediction. Leiva et al. (2024) demonstrated this sensitivity explicitly by incorporating a frother-dependent drag correction, showing that accounting for surfactant-induced changes in interfacial tension and bubble rigidity substantially improves predictive accuracy.

The hydrodynamic behavior of a rising bubble is governed primarily by the boundary condition at its gas-liquid interface. For a perfectly clean bubble, the interface is fully mobile, and tangential slip reduces drag relative to a rigid sphere, as captured analytically by the Hadamard-Rybczynski solution (Hadamard, 1911). In practice, however, clean bubble behavior is typically observed only for bubbles larger than approximately 0.7 mm in common aqueous systems. Below this threshold, even trace contaminants tend to immobilize the interface (Clift et al., 2005), making the fully mobile, uncoated bubble limit an upper bound on interfacial mobility that is rarely realized in industrial operations.

When surface-active species accumulate at the gas-liquid interface, Marangoni stresses progressively suppress tangential slip, driving the bubble from free-slip towards no-slip conditions and increasing drag toward the rigid-sphere limit. Azgomi et al. (2007) demonstrated that surfactant type affects terminal velocity not only by modifying bubble size but also by altering surface chemistry, while Navarra et al. (2008) showed that these effects extend to small bubbles with diameters below 1 mm. Critically, Acuña Pérez (2010) established that surfactant accumulation begins at bubble detachment and progresses during rise, so that initial velocity cannot be treated as terminal in the presence of surface-active agents.

Coated bubbles, also known as compound drops, represent a qualitatively distinct class: a gas core completely enclosed by an immiscible liquid shell which introduces its own viscosity, density, and interfacial tension into the force balance. Unlike bubbles with a molecular-scale surfactant layer, coated bubbles operate as a coupled, multi-scale system in which macro-scale shape, meso-scale viscous stress distribution, and micro-scale interfacial slip all interact simultaneously (Ji et al., 2022; Karp et al., 2021; S. Wang et al., 2018).

Existing drag correlations for uncoated bubbles in the intermediate Reynolds *(Re)* number range ($1 < Re < 1000$) are well established, with formulations by Tomiyama et al. (1998) and Yan et al. (2017) providing reliable predictions based on Re, Eötvös *(Eo)*, and Morton *(Mo)* numbers. For coated bubbles, analytical solutions by Johnson and Sadhal (1981; 1983, 1985) are restricted to Re much less than 1, and Kawano and Hashimoto (1997) extended these numerically to $Re < 200$. At higher Reynolds numbers, Ji et al. (2021, 2022) demonstrated that increasing the oil fraction progressively immobilizes the interface, altering the drag profile. In contrast, Karp et al. (2021) showed that compound-drop drag always exceeds that of an uncoated bubble at the same Reynolds number, even after an explicit viscosity-ratio correction.

Despite these advances, four critical gaps persist. First, no study has systematically varied both continuous-phase and coating viscosity across multiple fluid systems to isolate their independent effects. Second, existing models are either restricted to low Re or require the base drag coefficient as an input, with no unified absolute correlation that predicts C_D directly from dimensionless groups across the intermediate *Re* regime. Third, the viscosity ratio *(η)* has been examined only over narrow ranges, whereas industrial systems span values from below 1 to above 50. Fourth, the effects of coating fraction and viscosity ratio have never been statistically separated, as changing the oil type in prior studies simultaneously alters both parameters.

This work addresses these gaps by developing a unified empirical power-law correlation that predicts C_D directly from *Re, Eo, Mo,* the viscosity ratio, and coating fraction. Crucially, the formulation reduces to a standard three-parameter uncoated bubble model when no coating is present. The experimental matrix

spans three continuous phases and two organic phases, enabling the statistical separation of viscosity-ratio and coating-fraction effects. The resulting model is derived from 2,268 observations and validated against 25 independent external datasets comprising 2,910 bubble measurements. Within the validated operating window ($30 < Re < 1000$, $0.1 < Eo < 10$), the correlation provides an empirical drag closure suitable for single-bubble drift-flux and multiphase flow sub-models. Extension to turbulent, multi-bubble, or partially coated systems requires additional validation beyond the scope of the present work.

2. Hydrodynamics of single bubbles

The coupled effects of fluid properties, bubble deformation, and interfacial mobility dictate the rise dynamic of single bubbles. To establish the physical foundation for the drag model proposed in this study, the following sections review the force balance governing terminal velocity and the dimensionless groups controlling bubble dynamics.

2.1. Terminal velocity

The terminal velocity of a gas bubble rising through a stagnant liquid emerges from a dynamic equilibrium among buoyancy, gravity, and hydrodynamic drag. For a bubble of volume V_b, projected area A_p, and terminal velocity v_t. This equilibrium is expressed as Equation 1:

$$\rho_f V_b g - \rho_g V_b g = \frac{1}{2} C_D \rho_f A_p v_t^2 \tag{1}$$

where ρ_f is the continuous-phase density, ρ_g is the gas-phase density, g is gravitational acceleration, and C_D is the drag coefficient. This balance demonstrates that terminal velocity cannot be predicted solely from density differences and bubble geometry. The drag coefficient encapsulates the complex interactions between the bubble and the surrounding fluid. It acts as the controlling variable coupling bubble sizes, fluid properties, and interfacial characteristics into a single framework upon which all derived quantities, including residence time, gas holdup, and mass transfer rates, ultimately depend (Clift et al., 2005). The governing causal chain dictates that fluid properties determine the degree of bubble deformation and interfacial mobility; these factors together set the terminal velocity, from which the drag coefficient is derived.

In the Stokes regime ($Re < 1$), the drag force becomes linear in velocity, and the terminal velocity reduces to Equation 2 (Stokes, 1851):

$$v_t = \frac{(\rho_f - \rho_g) g d^2}{18\mu} \tag{2}$$

At intermediate Reynolds numbers ($1 < Re < 1000$), both boundary-layer dissipation and pressure drag contribute simultaneously. Because no analytical closed-form solution exists in this regime, the drag coefficient must be determined via empirical correlations or numerical simulation. This intermediate regime is of primary practical relevance for bubbles in industrial systems (Clift et al., 2005; Tomiyama et al., 1998).

The total drag on a rising bubble comprises two contributions. Viscous drag arises from tangential shear stress at the bubble surface. It dominates at low *Re*, where interfacial mobility has the greatest influence. Pressure drag arises from an asymmetric fore-aft pressure distribution caused by flow separation and wake formation. It becomes dominant at intermediate and high *Re* (Lee & Park, 2017). In the regime relevant to this work ($30 < Re < 1000$), both mechanisms interact dynamically. An oil coating increases the viscous contribution by suppressing interfacial slip, while simultaneously modifying pressure drag through alterations in effective density, interfacial tension, and wake dynamics. The relative weight of these two mechanisms shifts with *Re* and *Eo*, and their combined effect is what the empirical exponents in the drag correlation ultimately capture (Yan et al., 2017).

2.2. Dimensionless numbers that govern the movement and shape of bubbles

Three dimensionless groups govern bubble movement and shape in the intermediate regime. The Reynolds number (*Re*) quantifies the ratio of inertial to viscous forces and determines the local flow structure around

the bubble. The Eötvös (*Eo*) number quantifies the competition between gravitational deformation and surface-tension resistance: at $Eo < 0.2$, bubbles remain spherical; near $Eo \sim 1$, they deform into oblate ellipsoids; and at $Eo > 10$, they develop cap-like or fragmenting shapes (Bhaga & Weber, 1981; Clift et al., 2005). This deformation increases the projected area generating additional form drag. The Morton number (*Mo*) (Haberman & Morton, 1953; Pfister & Hager, 2014) is a fluid-property group that aggregates the coupled effects of viscosity, surface tension, and density difference. Because *Mo* depends exclusively on fluid properties rather than bubble size or velocity, it functions as a fluid-classification parameter that characterizes the continuous phase independently of the specific bubble under consideration. Consequently, *Re* and *Eo* are treated throughout this work as the primary control parameters governing drag, while *Mo* establishes the fluid-property context within which those parameters operate (Tadaki & Maeda, 1961). These three groups are mathematically related through $We^2 = Re^4 \cdot Mo \cdot Eo$, confirming that they constitute a complete and independent set for this hydrodynamic problem (Yan et al., 2017). These dimensionless groups are summarized in Table 1.

Table 1. Dimensionless numbers used in the paper

Dimensionless Number	Physical Meaning
Reynolds ($Re = \frac{\rho_f v_t d}{\mu}$)	Inertia vs. viscosity
Eötvös ($Eo = \frac{\Delta\rho g d^2}{\sigma}$)	Gravity vs. surface tension
Morton ($Mo = \frac{\Delta\rho g \mu^4}{\rho_f^2 \sigma^3}$)	Coupled viscous-capillary effects
Weber($We = \frac{\rho v_t^2 d}{\sigma}$)	Inertia vs. surface tension

For uncoated bubbles, σ is the gas-liquid surface tension, d is the bubble diameter, and $\Delta\rho$ is the gas-liquid density difference. For coated bubbles, σ is the organic-continuous interfacial tension, d is the coated bubble diameter, and $\Delta\rho$ is the apparent density of the compound object. In both cases, μ is the viscosity of the continuous phase. This consistent definition allows uncoated and coated bubbles to be described within a single, unified dimensionless framework.

2.3. Interfacial mobility and Marangoni effects

The drag force acting on a rising bubble depends critically on the mobility at its gas-liquid interface. At one extreme, a perfectly clean interface permits full tangential slip: gas recirculates internally, the no-penetration condition is satisfied, but the no-slip condition is not, and drag is substantially reduced relative to a rigid sphere (R. Chen et al., 2026). At the other extreme, a fully immobilized interface behaves as a no-slip boundary, and bubble drag approaches the rigid-sphere limit. Between these limits lies a continuous spectrum of partial immobilization, which is determined by the concentration and type of surface-active species present, the bubble size, and the time elapsed since bubble formation (Acuña Pérez, 2010). The transition from free-slip to no-slip is not instantaneous; it develops progressively as surfactants accumulate along the interface during the bubble's rise. This accumulation creates a non-uniform surface-tension distribution that generates tangential Marangoni stresses opposing the direction of the surface flow. Ultimately, the flow on the surface can be considered the result of competition between gravity-driven drainage and Marangoni stress (Acuña et al., 2008).

Marangoni stresses arise from surface-tension gradients across the bubble interface. As a bubble rises, surfactant molecules are swept by the internal flow toward the rear of the bubble, creating a local concentration gradient and a corresponding variation in surface tension that opposes further surface motion. The resulting stress immobilizes the interface, suppressing the internal circulation that characterizes uncoated bubbles and progressively driving drag toward the rigid-sphere limit. The

magnitude of this effect depends on surfactant type and concentration: Azgomi et al. (2007) demonstrated that different surfactants produce distinct drag responses even at equivalent bulk concentrations, reflecting differences in adsorption kinetics and surface rheology. R. Chen et al. (2026) further demonstrated, using particle image velocimetry measurements, that surfactant-induced Marangoni stresses create spatially heterogeneous boundary conditions across the bubble surface, transitioning dynamically from free-slip at the front to no-slip at the rear pole. These stresses promote early flow separation and establish a distinct stagnant wake zone that contributes additional form drag. Because these interfacial effects are not captured by classical drag correlations derived under the assumption of uniform boundary conditions, their omission represents a systematic source of predictive error in both contaminated and coated bubble systems.

2.4. Coated bubble systems

Coated bubbles exhibit drags profiles that fall between those of uncoated bubbles and rigid spheres, depending on the coating viscosity, coating fraction, and viscosity ratio. Analytical solutions by Johnson and Sadhal (1981, 1985) place compound-drop drag strictly between the classic Hadamard-Rybczynski and rigid-sphere limits at Re much less than 1. Subsequently, Kawano and Hashimoto (1997) extended these numerically to $Re < 200$, introducing a mobility parameter $B = (1 + 3\kappa b)/(1 + 2\kappa b)$, where κ is the film-to-continuous viscosity ratio, and b is a geometric parameter dependent on film thickness. This parameterization effectively quantifies the degree of interface immobilization as a direct function of the coating's physical properties.

At higher Reynolds numbers ($Re \sim 60 - 100$), Ji et al. (2021, 2022) demonstrated that increasing the oil volume fraction monotonically reduces the drag coefficient, suppresses path oscillations, and progressively shifts the interface boundary condition, and progressively shifts the interfacial boundary condition from free-slip towards no-slip. S. Wang et al. (2018) observed lower rise velocities, weaker shape deformation, and smaller oscillation amplitudes in coated bubbles, noting behaviors analogous to surfactant-contaminated systems. In contrast, Karp et al. (2021) reported that the drag of coated bubbles consistently exceeds that of uncoated bubbles at equivalent Re numbers, with greater scatter in oscillatory trajectories.

Bubble deformation plays a central and independent role in determining drag, distinct from the effects of interfacial mobility and viscosity ratio. As the Eötvös (Eo) number increases beyond $Eo > 0.2$, the bubble transitions from a spherical to an oblate ellipsoidal shape, increasing the projected area normal to the flow vector and shifting the stagnation pressure distribution. This geometric transition alone increases drag through two coupled mechanisms: first, the larger projected area directly amplifies the pressure force resisting motion; second, the flattened rear surface promotes earlier flow separation, enlarging the low-pressure wake region and amplifying form drag.

In coated bubbles, deformation is governed by the Eötvös number computed using the apparent density difference and interfacial tension of the compound object, whereby the oil shell modifies the deformation state relative to an uncoated bubble of the same gas-core volume. A thicker or denser oil shell increases the apparent density difference and reduces the effective interfacial tension, both of which consequently raise the Eötvös number, promoting a more pronounced deformation.

3. Materials and experimental methods

The experimental design integrated a combination of distinct fluid systems with a specialized coated-bubble generation apparatus and a high-speed image analysis system. This was utilized to determine bubble properties such as equivalent diameter, inclination angle, and terminal velocity. Thereby enabling systematic evaluation of the coupled effects of viscosity ratio, interfacial properties, and bubble deformation across the intermediate Reynolds number (Re) regime.

3.1. Fluid properties

Experiments were conducted across nine fluid combinations, comprising three continuous phases and two organic phases, selected to span a wide range of physical property ratios while satisfying the

thermodynamic criterion for spontaneous oil coating. The three continuous phases were tap water, sodium chloride solution (NaCl, 26 wt%), prepared from reagent-grade NaCl (≥99% purity, Sigma-Aldrich) dissolved in tap water, and sucrose solution (sucrose, 30 wt%), reagent grade (≥99% purity, Sigma-Aldrich), providing continuous-phase viscosities(μ) of 1.0, 2.2, and 5.9 mPa·s, and surface tensions of 72.8, 80, and 75 mN/m, respectively. The two organic phases were kerosene and sunflower oil, possessing dynamic viscosities of 1.99 and 58 mPa · s. This combination provided a spectrum of film to continuous phase viscosity rations, defined as $\eta = \mu_{oil}/\mu_{f.}$ The resulting experimental array spans viscosity ratios from η = 0.34 (kerosene in sucrose solution) to η =58 (sunflower oil in water). This broad range successfully captures the transition from coatings less viscous than the continuous phase to those that are substantially more viscous, enabling systematic investigation of viscosity-ratio effects on hydrodynamic drag.

It should be noted that the term "uncoated bubble" is used throughout this work strictly to denote the oil-free baseline from oil-coated compound bubbles. This designation does not imply a perfectly "clean" interface in the classical sense of Legendre et al. (2012) or P.C. Duineveld (1995). Instead, it distinguishes the baseline from the oil-coated bubbles investigated in this study, rather than a surfactant-free one from a contaminated one. Consequently, the drag correlation developed in this study should be understood as valid for this contaminated-interface condition, representative of tap water and typical industrial process water, rather than idealized, ultra-pure fluid systems. The continuous phases used (26 wt% NaCl, 30 wt% sucrose, and tap water) contain trace background contaminants that may partially immobilize the gas-liquid interface. Accordingly, the baseline drag behavior is expected to fall between the analytical Hadamard-Rybczynski (fully mobile) and rigid-sphere (fully immobilized) limits, consistent with established contaminated interface models in the literature (J. Chen et al., 2019; Tomiyama et al., 1998)

Liquid Densities were measured using a calibrated pycnometer under temperature controlled conditions, with an estimated experimental uncertainty of ±0.5 kg · m^{-3}. Surface tension was determined via the Du Noüy ring method, with an associated measurement error of ±0.05 mN · m^{-1}. Dynamic viscosities were measured with a capillary viscometer, with an associated uncertainty of approximately ±2% of the recorded value. All physical property measurements were performed in triplicate, and the reported values correspond to the average of these independent experimental determinations.

The equilibrium configuration of a three-phase system comprising gas, oil, and water is determined by the three spreading coefficients, defined generally as $S_i = \sigma_{jk} - (\sigma_{ij} + \sigma_{ik})$ (Gomez et al., 2001; Tarkan & Finch, 2005). For spontaneous complete coverage of the gas core by an oil shell in a continuous aqueous phase, the spreading coefficient of the oil phase (S_c) is $S_c = \sigma_{ag} - (\sigma_{oa} + \sigma_{og}) > 0$. Here, the subscripts a, g, and o denote the aqueous, gas, and organic phases, respectively. All six oil-coating systems investigated in this work satisfy this thermodynamic requirements $Sc > 0$, confirming that complete oil encapsulation of the gas core is thermodynamically favorable across all tested fluid combinations. The full set of fluid properties and spreading coefficients for all nine experimental conditions is reported in Table 2.

3.2. Coated bubble generation system

Experiments were conducted in a vertical acrylic column of 1.0 m in height, providing a sufficient rise distance for bubbles in the 1.0 – 5.0 mm diameter range to reach terminal velocity under all tested continuous-phase conditions. To capture the bubble kinematics, a localized acrylic observation box (0.15m x 0.05m x 0.30m) was mounted near the first column. Optical calibration was achieved via physical scale bars mounted within the camera's depth of field. Illumination was provided by a non-flickering A21 light bulb (Waveform Lighting®) with a color rendering index of 95, an output of 1600 lumens, and a diffuser positioned behind the acrylic box to ensure uniform backlighting and minimize optical artifacts in bubble detection.

Coated bubbles were generated using a needle-based coaxial orifice system, designed according to the principles established by Hayakawa and Shigeta (1974) and Ji et al. (2021). In this configuration, an inner needle is positioned inside a coaxial tube; the gas phase is injected through the inner needle, while the organic phase is simultaneously metered through the surrounding annulus. This arrangement ensures

Table 2. Fluid properties for all nine experimental conditions, a= aqueous, g=gas, o=organic

Exp	ρ_a (kg/m³)	μ_a (mPa s)	σ_{ag} (mN/m)	ρ_o (kg/m³)	μ_o (mPa s)	σ_{oa} (mN/m)	S_c (mN/m)	η
Water_Kerosene	990	1	72.8	797	1.99	40	7.80	1.99
Water_Oil	990	1	72.8	912	58	26	14.80	58.00
Water_Air	990	1	72.8					
Salt_Air	1185	2.2	80					
Salt_Kerosene	1185	2.2	80	797	1.99	50	5.00	0.91
Salt_Oil	1185	2.2	80	912	58	36	12.00	26.36
Sugar_Kerosene	1172	5.9	75	797	1.99	45	5.00	0.34
Sugar_Oil	1172	5.9	75	912	58	29	14.00	9.83
Sugar_Air	1172	5.9	75					

complete encapsulation of the gas core by the oil at the point of detachment. Uncoated bubbles were generated by injecting air through the same submerged coaxial orifice without an organic phase flow. The entire assembly was positioned 2–3 mm above the column base. Fig. 1 presents the experimental set up utilized in this research, and Fig. 2 illustrates the time sequence of coated-bubble formation for a representative kerosene-coated case. While a column height of 1.0 m proved fully adequate for terminal velocity equilibration within the tested 1.0 – 5.0 mm diameter range, a height of at least 1.5m would be required to fully characterized extended path oscillation cycles for the largest bubble cohorts.

3.3. Imaging and velocity measurements

Bubble trajectories, projected areas, and volumes were extracted from high-speed video sequences recorded at 120 fps with spatial resolutions ranging from 30 to 50 pixels · mm^{-1}. Images were preprocessed by subtracting a static background computed as the median of 50 bubble-free frames,

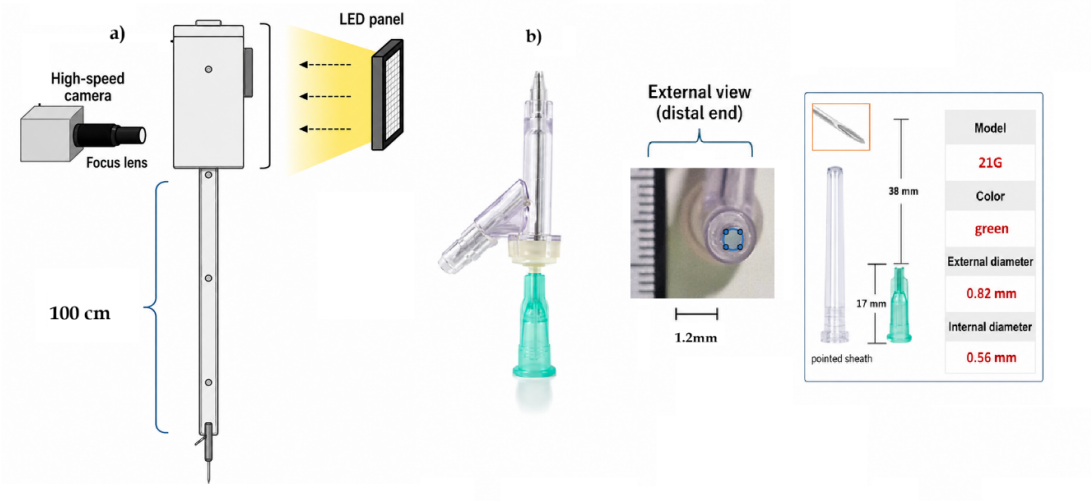

Fig. 1. Experimental setup for coated-bubble generation and imaging: (a) High-speed imaging system, comprising a high-speed camera with focusing lens aligned across the 1.0 m column against a diffuse LED backlight panel; (b) Coaxial needle-in-tube assembly used to generate coated bubbles, detailing the pointed outer sheath (organic-phase channel) and inner 21 gauge (*21G*) needle (gas channel; green hub, 0.82 mm external / 0.56 mm internal diameter), together with a magnified external view of the distal (submerged) tip showing the square gas-core cross-section (1.2 mm) at the orifice

Fig. 2. Time sequence showing the formation process of a kerosene coated bubble

and the resulting frames were converted to grayscale. Binary segmentation was performed using a thresholding method, followed by morphological closing with a disk shaped structuring element of (radius 3 pixels) to fill small gaps in bubble contours. Connected components were identified using MATLAB's regionprops function, and objects touching the image border or smaller than 50 pixels² were systematically rejected. For coated bubbles, where the oil layer and gas core produce different contrast levels, a two-pass segmentation workflow was applied: first at a lower threshold to capture the full coated-bubble envelope, and then at a higher threshold to isolate the brighter gas core. The regionprops function extracted the major and minor axes, centroid, and orientation angle for each detected object in each frame.

Bubbles were accepted for analysis if they satisfied five criteria. First, the air-core volume fraction (φair) ranged from 0.2 to 0.93, corresponding to the range where the oil coating forms a continuous shell. Second, the bubble contained a single connected gas core, with multi-core clusters rejected. Third, the bubble trajectory remained within the central 60% of the column cross-section to avoid wall effects. Fourth, the bubble was tracked for at least 10 consecutive frames to ensure a statistically meaningful average velocity. Fifth, the standard deviation of both velocity and bubble diameter remained below 10% of their respective mean values. Of the more than 3,000 bubbles initially detected, approximately 2,268 passed all five filters. Fig. 3 illustrates the selection criteria applied to representative bubbles from the water-kerosene experiment, showing an accepted coated bubble alongside examples of rejected ones for exceeding the maximum φair threshold and for containing a cluster of air bubbles. In addition to these five acceptance criteria, terminal velocity attainment was confirmed for each accepted bubble by verifying that the frame-to-frame vertical velocity showed no systematic drift (i.e., no monotonic increase or decrease) across the tracking window distinguishing true terminal transport from bubbles still accelerating when they entered the field of view

Since the drag coefficient (C_D) is derived directly from terminal velocity measurements via Equation 3, any experimental uncertainty in v_t propagates into the calculated C_D value. From Equation 3, C_D scales as v_t^{-2}, a relative uncertainty of $\delta v_t/v_t$ in the terminal velocity produces a corresponding relative uncertainty of approximately $2\delta v_t/v_t$ in the drag coefficient. Given the strict data acceptance criterion, which restricts the standard deviation to below 10% of the mean velocity, the maximum propagated uncertainty in C_D from velocity measurement alone is bounded at approximately 20%. In practice, the observed coefficient variation in $C_D$ranges from 0.8% to 9.7% across all experimental runs. Due to these values falling substantially below the theoretical 20% upper bound, it indicates that bubble-to-bubble variability in size and shape is the dominant driver of data scatter rather than random velocity measurement errors within individual bubble tracks. Uncertainty contributions from projected area (A_p) measurement, which enters C_D linearly through A_p in Equation 3, were evaluated by executing repeated segmentation routines on identical image sequences and found to contribute to less than 3% relative uncertainty under the applied acceptance criteria.

3.4. Drag coefficient calculation

The drag coefficient (C_D) is not a directly measurable quantity; it must be derived from the terminal velocity (v_t), which is the primary experimental observable. In this study, C_D was computed directly from the force balance at terminal velocity, using the bubble volume and the projected area normal to the rising direction, rather than deriving it from an assumed equivalent spherical diameter. This approach avoids the distortion

of shape characteristics introduced by the spherical approximation and is expressed as Equation 3, which is a rearrangement of Equation 1:

$$C_D = \frac{2Vg(\rho_f - \rho_g)}{\rho_f v_t^2 A_p} \tag{3}$$

Fig. 3. Detection algorithm selection criteria for bubbles in a Water-Kerosene solution, from left to right: (A) accepted coated bubble with φair = 0.48, (B) rejected coated bubble for exceeding φ_{air}, and (C) rejected bubble for having a cluster of air bubbles

where V is the bubble volume, g is gravitational acceleration, ρ_f and ρ_g are the continuous-phase and gas densities, v_t is the terminal velocity, and A_p is the bubble's projected area normal to the direction of rise. For coated bubbles, the effective interior density $\rho_{eff} = \rho_{air}\,\varphi_{air} + \rho_{oil}\,\varphi_{oil}$ accounts for the mass of both the gas core and the oil shell, and the oil volume fraction $\varphi_{oil} = 1 - \varphi_{air}$ is obtained directly from the measured volumetric air fraction in the images.

For non-spherical bubbles, an appropriate equivalent diameter must be defined before the drag coefficient can be computed. The most common approach employs the equivalent spherical diameter corresponding to the same volume (Equation 4), where a and b denote the major and minor semi-axes of the oblate spheroid:

$$d_b = \sqrt[3]{(2a)^2 2b} \tag{4}$$

However, this conventional approach neglects variations in the projected area of an oblate spheroid and masks shape dependent geometric information that significantly influences hydrodynamic behavior. For a sphere, the ratio between volume (V) and projected area (A_p) yields a consistent equivalent diameter as shown in Equation 5, directly from the sphere relation $V/A_p = 2d/3$:

$$d_b = \frac{3}{2}\frac{V_{sphere}}{A_{p,sphere}} \tag{5}$$

For ellipsoidal and oblate spheroidal shapes, the assumptions of spherical symmetry no longer hold, and the volume-only equivalent diameter of Equation 4 is therefore inadequate. Consequently, the equivalent diameter defined by Equation 5, which relates volume to projected area, is adopted for oblate spheroids throughout this work, preserving the geometric information relevant to drag computation.

The oblate spheroid is the relevant geometry for deformed bubbles in the intermediate Reynolds number regime (56–894 in the present dataset; commonly taken as $1 < Re < 1000$ in the broader literature). This shape arises when a sphere is compressed along its polar axis and expanded along its equatorial axis, with volume and projected area given respectively by (Equation 6 and Equation 7):

$$V = \frac{4}{3}\pi a^2 b \tag{6}$$

$$A_{p,OS} = \frac{\pi\, a^2\, b}{\sqrt{a^2\,(\sin\alpha)^2 + b^2\,(\cos\alpha)^2}} \tag{7}$$

where a and b are the equatorial and polar semi-axes, and α is the inclination angle of the bubble with respect to the horizontal axis. When the bubble rises without tilt, the projected area corresponds directly to

the axisymmetric cross-section normal to the direction of motion. When the bubble is inclined, the projected area must be corrected by the inclination angle to preserve orthogonality with the rising direction. The equivalent diameter used throughout this work is then computed from Equation 5 using the volume from Equation 6 and the inclination-corrected projected area from Equation 7, ensuring that both shape and orientation are properly accounted for in the drag coefficient calculation.

3.5. Experimental design and dimensionless ranges

The nine experimental conditions are summarized in Table 3. The experiment label encodes the continuous and organic phases and serves as the primary lookup key throughout the analysis. Conditions *3*, *4*, and *9* are uncoated bubble baselines for the water, salt, and sucrose continuous phases, respectively; conditions *1*, *2*, *5*, *6*, *7*, and *8* are oil-coated compound bubble experiments. For each coated condition, the corresponding uncoated bubble baseline serves as the reference against which the oil coating's drag modification is evaluated. The full fluid properties for each experimental condition, including density, viscosity, interfacial tension, spreading coefficient, and viscosity ratio, are reported in Table 2.

These experimental conditions collectively span a wide range of dimensionless parameter space. Reynolds numbers range from approximately 56 to 894, covering the lower intermediate regime in the sucrose phase systems and extending up to the upper intermediate regime in the water phase uncoated bubble baseline. Eötvös numbers span from 0.27 to 9.94, encompassing spherical, oblate ellipsoidal, and near cap bubble shapes within a single dataset. Morton numbers range from 2.57×10^{-11} (water) to 2.81×10^{-7} (sucrose solution), reflecting the wide variation in continuous phase viscosity and surface tension across the three aqueous systems. Viscosity ratios range from 0.34 (kerosene in sucrose solution) to 58 (sunflower oil in water), enabling investigation of coating effects across regimes in which the oil layer is less viscous, equally viscous, or substantially more viscous than the continuous phase. This parameter range ensures the resulting correlation is not specific to a single fluid system but reflects the broader hydrodynamic behavior of coated bubbles across industrially relevant conditions.

Table 3. Nine-condition experimental matrix. The label indicates the name of each experiment and the baseline/reference points to which the experiment is related.

Exp #	Label	Continuous phase	Organic phase	Bubble type	Baseline, reference
1	Water_Kerosene	Tap water	Kerosene	Compound	3
2	Water_Oil	Tap water	Sunflower oil	Compound	3
3	Water_Air	Tap water		Uncoated bubble	
4	Salt_Air	NaCl 26 wt%		Uncoated bubble	
5	Salt_Kerosene	NaCl 26 wt%	Kerosene	Compound	4
6	Salt_Oil	NaCl 26 wt%	Sunflower oil	Compound	4
7	Sugar_Kerosene	Sucrose 30 wt%	Kerosene	Compound	9
8	Sugar_Oil	Sucrose 30 wt%	Sunflower oil	Compound	9
9	Sugar_Air	Sucrose 30 wt%		Uncoated bubble	

4. Results and discussion

The dataset comprises 2,268 accepted individual bubble observations distributed across nine experimental conditions: 103 (Water-Kerosene), 61 (Water-Oil), 656 (Water-Air), 570 (Salt-Air), 66 (Salt-Kerosene), 248 (Salt-Oil), 173 (Sugar-Kerosene), 219 (Sugar-Oil), and 172 (Sugar-Air). Table 4 reports the mean and standard deviation of bubble diameter, drag coefficient, and terminal velocity for each experimental condition. Coated bubbles are systematically larger than their gas cores: the mean coated diameter exceeds the mean air-core diameter by 30–75%, depending on the oil fraction and organic phase. The coefficient of variation in C_D ranges from 0.8% (Sugar-Oil) to 9.7% (Salt-Oil), reflecting the damping effect of the continuous phase viscosity on bubble shape oscillations and path instability.

Coated bubbles rise more slowly than uncoated bubbles in water and salt systems, with mean velocities of 13.3 and 13.2 cm/s in Water-Kerosene and Water-Oil, respectively, versus 21.3 cm/s for Water-Air, and 17.9–19.2 cm/s in Salt-coated systems versus 23.4 cm/s in uncoated systems. The sucrose system shows the opposite trend, with coated bubbles exceeding the uncoated baseline velocity, consistent with the low viscosity ratio, in which the oil layer reduces rather than increases interfacial resistance. All experiments fall within the intermediate *Re* regime (56 - 894). Fig. 4 presents terminal velocity as a function of bubble diameter.

Table 4. Summary statistics by experiment: mean coated diameter, mean drag coefficient, and mean v_t for all measurements in each experiment, along with the mean standard deviation (STD) for each value.

Exp #	Label	N	Mean d_b(mm)	STD d_b(mm)	Mean C_D	STD C_D	CV% C_D	Mean v_t(cm/s)	STD v_t (cm/s)
1	Water_Kerosene	103	2.47	0.05	0.99	0.03	3%	13.28	0.18
2	Water_Oil	61	2.95	0.06	1.07	0.04	4%	13.17	0.15
3	Water_Air	656	2.49	0.06	0.76	0.04	5%	21.30	0.36
4	Salt_Air	570	2.77	0.10	0.67	0.05	7%	23.41	0.59
5	Salt_Kerosene	66	3.84	0.29	0.98	0.07	7%	17.96	0.23
6	Saltl_Oil	248	4.47	0.41	0.92	0.09	10%	19.24	0.29
7	Sugar_Kerosene	173	3.11	0.05	0.62	0.01	2%	20.91	0.07
8	Sugar_Oil	219	4.02	0.03	0.52	0.00	1%	23.68	0.06
9	Sugar_Air	172	2.13	0.01	0.88	0.00	0.8%	17.85	0.05

4.1. Drag behavior

The three uncoated bubble experiments provide the drag reference against which all oil coated conditions are evaluated. When plotted as C_D versus Reynolds number, these three baselines trace distinct trajectories that reflect the different continuous phase properties. The Water-Air baseline spanning $207 \leq Re \leq 809$, shows C_D values ranging from approximately 0.60 at high *Re* to 0.93 at the lowest *Re*, where bubble shape deformation and path oscillations become significant. The Salt-Air occupies $252 \leq Re \leq 430$ systematically displays lower C_D values (0.61 - 0.85) compared to the Water-Air baseline at comparable Reynolds numbers. This is consistent with the higher surface tension of the salt solution (σ = 80 mN/m versus 72.8 mN/m for water), which reduces bubble deformation and hence form drag. The Sugar-Air baseline is confined to a narrow band near $56 \leq Re \leq 100$, showing the highest C_D values in that range (0.67–1.05), consistent with the elevated continuous-phase viscosity of 5.9 mPa · s. Fig. 5 shows the experimental drag coefficient as a function of Reynolds number for all experiments with their respective error bars.

Because the three uncoated baselines occupy different, only partially overlapping Reynolds number windows, as well as C_D itself scales strongly with Re (exponent ≈ −2.0 in Equation 9), mean C_D values were recomputed for each coated condition and its corresponding uncoated baseline restricted to their common, overlapping Re window (Table 5); isolating the coating effect from the effect of operating at different Reynolds numbers. Once Re is controlled, the drag increases in the water system becomes predominantly confined to the higher viscosity sunflower oil coating, whereas the lower viscosity kerosene coating yields a negligible net change. The salt and sucrose systems retain their coating effect, increase and reversal respectively, and in both cases it is larger than the unmatched, system-wide means suggested.

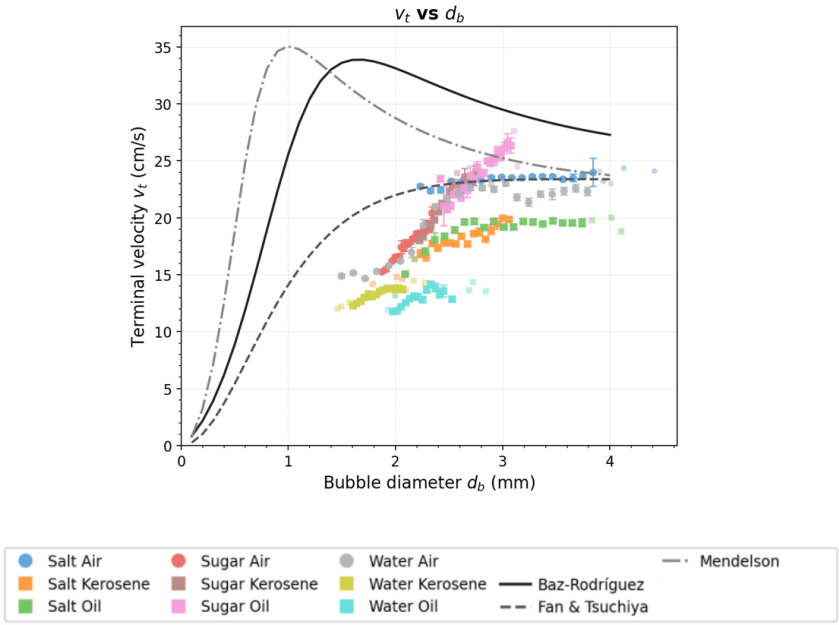

Fig. 4 Results for terminal velocity of bubbles and coated bubbles, equations for the models are in Appendix A.2

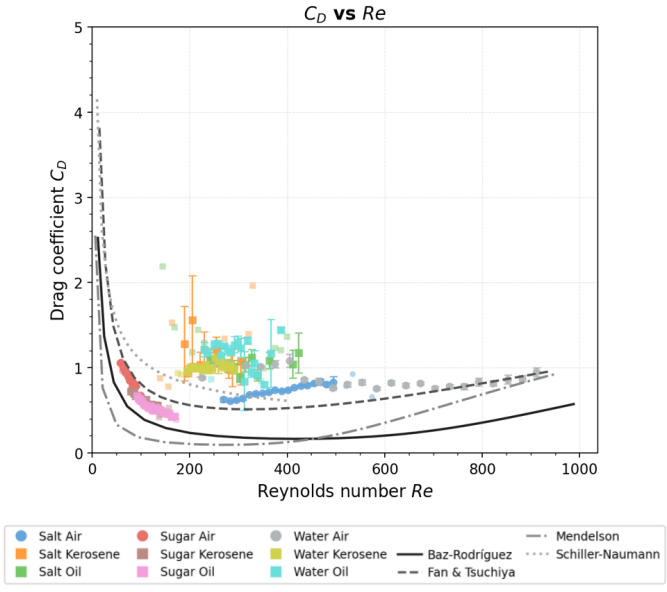

Fig. 5. Results for the drag coefficients of uncoated and coated bubbles; the continuous line is derived from the terminal velocity models in Appendix A.2.

Table 5. Reynolds-matched drag coefficient comparison

Continuous phase	Coating	Overlapping Re window	n (baseline)	C_D (baseline)	n (coated)	C_D (coated)	ΔC_D
Water	Kerosene	210–325	67	1.033	85	1.026	−0.7%
Water	Sunflower oil	226–390	94	1.038	84	1.156	+11.4 %
Salt	Kerosene	263–333	82	0.661	34	1.194	+80.6 %
Salt	Sunflower oil	263–429	488	0.720	264	1.033	+43.4 %
Sucrose	Kerosene	69–100	132	0.849	129	0.660	−22.3 %
Sucrose	Sunflower oil	81–100	50	0.800	42	0.587	−26.6 %

The sucrose system presents qualitatively different behavior: both Sugar-Kerosene (C_D = 0.62, full-range mean) and Sugar-Oil (C_D = 0.52, full-range mean) show lower drag coefficients than the Sugar-Air baseline (C_D = 0.88, full-range mean), consistent with the Reynolds-matched reversal already reported in Table 5 (−22.3% and −26.6%, respectively). This provides strong experimental evidence that drag modification by oil coating is not universally monotonic. The viscosity ratio appears to be a secondary factor within the tested parameter range $0.34 \leq \eta \leq 58$, though this range is defined by only two organic phases (Section 4.2). In a high viscosity continuous phase, the oil layer reduces effective interfacial resistance relative to the uncoated gas-liquid interface, a mechanism not captured by existing correlations developed for low-viscosity continuous phases.

Comparing coated conditions within the same continuous phase isolates the viscosity ratio effect. In the water system, kerosene (η = 1.99) and sunflower oil (η = 58) differ by only 8% in mean C_D, despite a viscosity ratio of 29. These results confirm that the viscosity ratio is a secondary contributor to drag modification, with *Re* and *Eo* remaining dominant.

The effect of coating fraction on drag is assessed through the distribution of φ_{air} values within each coated experiment. Across all six coated conditions, bubbles with larger oil shells (lower φ_{air}) do not exhibit a consistent increase in relative to bubbles with thinner coatings within the same experiment. The coating fraction exerts a statistically detectable but modest influence on drag, with a tenfold increase in oil fraction producing an estimated 18% reduction in C_D within the coated-bubble model. Part of this effect is already implicitly captured by the Eötvös and Morton numbers, which incorporate the apparent density and interfacial tension of the coated bubble and therefore indirectly reflect changes in coating fraction. The combined evidence from viscosity ratio and coating fraction analyses confirms that the dominant controls on drag in coated bubble systems are *Re* and *Eo*, with *Mo* providing the continuous-phase context, and that coating-specific parameters act as secondary modifiers within the tested range. These findings provide the empirical basis for model development.

4.2. Dimensionless formulation

Before presenting the regression results, the physical expectations are: *Re* carries a strong negative exponent reflecting viscous-to-inertial transition; *Eo* carries a positive exponent as deformation increases projected area and form drag; *Mo* carries a negative exponent as higher viscosity suppresses wake instabilities; coating fraction contributes a modest negative exponent; and viscosity ratio is expected to be secondary since *Mo* captures most continuous-phase viscosity information.

Empirical correlations were developed by regressing C_D on *Re*, *Eo*, *Mo*, η (coating-to-continuous viscosity ratio), and φ_{air} (Equation 8), with ordinary least squares used to fit the prefactor *A* and exponents a through

e. For uncoated bubbles, η = 1 and φ_{air} = 1, reducing the model to a three-parameter power law. Three correlations were fitted: uncoated bubble (1,398 observations), coated bubble (870 observations), and unified (2,268 observations).

$$C_D = A^* Re^a * Mo^b * Eo^c * \eta^d * \varphi_{air}^e \quad (8)$$

A structural coupling exists between the drag coefficient and the Reynolds number: both quantities are derived from the same measured terminal velocity vt, with $C_D \propto v_t^{-2}$ (Equation 3) and $Re \propto v_t$. This shared dependence means that part of the observed goodness-of-fit may reflect the mathematical relationship between C_D and Re rather than purely independent predictive power. This coupling is inherent to all empirical drag correlations for freely rising bubbles, including those of Tomiyama et al. (1998) and Yan et al. (2017) against which the present model is compared, and is not unique to the current approach. The reported R^2 values should therefore be interpreted as measures of the quality of the power-law fit within the training data rather than as unconditional measures of predictive independence. The validation against 25 independent external datasets (Section 4.3), where model predictions are compared to observations from independent measurement campaigns with no parameter sharing, provides a more conservative assessment of predictive performance and confirms that the correlation retains a mean *MAPE* of *5 – 6%* under fully out-of-sample conditions. Consequently, the internal $R^2 = 0.97$ reported for the regression should not, by itself, be read as a measure of forecasting skill; the external-validation *MAPE* of *5 – 6%* (Section 4.3, 25 independent datasets with no shared parameters) is the more appropriate Fig. for assessing the correlation's predictive capability. Table 6 reports estimates, standard errors, t-statistics, p-values, and 95% confidence intervals for the unified model

The uncoated bubble correlation was derived from 1,398 observations spanning the three uncoated bubble baseline experiments (Water-Air, Salt-Air, Sugar-Air), covering Reynolds numbers from 56 to 894 and Eötvös numbers from 0.27 to 1.71. The resulting power-law model is given by Equation 9:

$$C_D = 3.8 * Re^{-2.04} * Mo^{-0.51} * Eo^{1.54} \quad (9)$$

The exponents are physically consistent: negative *Re* reflects the viscous to inertial transition, positive *Eo* captures the deformation driven increase in form drag, and negative *Mo* is consistent with viscosity-mediated suppression of wake instabilities. For uncoated bubbles, η and φ_{air} are set to unity, effectively reducing the correlation to a three parameter power law while retaining formal consistency with the unified expression. Statistical performance is reported in Table 7.

The coated-bubble correlation (Equation 10) was derived from 870 observations covering *Re* = 96–860 and *Eo* = 0.48–9.94. The *Re*, *Mo*, and *Eo* exponents differ by less than 2% from those of the uncoated bubble model, suggesting that the dominant hydrodynamic scaling is preserved across both regimes. The viscosity ratio exponent ($\eta^{0.002}$) is negligibly small, reflecting statistical redundancy once *Re* and *Mo* are included. In contrast, the coating fraction exponent ($\varphi_{air}^{-0.07}$) indicates a modest drag reduction with increasing oil shell thickness.

$$C_D = 1.6 * Re^{-2.08} * Mo^{-0.53} * Eo^{1.53} * \eta^{0.002} * \varphi^{-0.07} \quad (10)$$

The unified drag model captures the central physical result of this work: that uncoated and coated bubbles obey the same drag scaling laws, differing only in the prefactor that reflects the degree of interfacial immobilization imposed by the oil shell. Derived from all 2,268 observations, the unified correlation is (Equation 11):

$$C_D = 1.3509 * Re^{-2.023} * Mo^{-0.514} * Eo^{1.488} * \eta^{-0.002} * \varphi^{-0.039} \quad (11)$$

The exponents for *Re*, *Mo*, and *Eo* remain consistent with those of both individual models, supporting the robustness of the underlying hydrodynamic scaling across the full dataset. The unified model reduces to a three-parameter uncoated bubble correlation when no coating is present (η = 1, φ_{air} = 1), providing a seamless transition between uncoated and coated regimes within a single equation. Table 7 presents the statistical results broken down by experiment.

The statistical significance of all regression exponents was assessed by ordinary least squares inference.

Table 6 OLS regression statistics for the unified model (Equation 11), n = 2,268:

Parameter	Estimate	Std. Error	T	p-value	95% CI
A	1.3509	—	14.98	<2.2 $10^{-}1^{6}$	[1.299, 1.405]
a (Re)	−2.0233	0.0079	−255.5	< 2.2×10^{-16}	[−2.038, −2.0077]
b (Mo)	−0.5143	0.0018	−279.1	< 2.2×10^{-16}	[−0.5179, −0.5106]
c (Eo)	1.4883	0.0056	264.7	< 2.2×10^{-16}	[1.4773, 1.4994]
d (η)	0.002	0.0007	−0.02	0.984	[−0.0486, −0.0288]
e (φair)	−0.0387	0.005	−7.66	2.7×10^{-14}	[−0.0015, +0.0014]

The -values in Table 6 reflect point-level inference and should be interpreted with appropriate caution. Although the regression was fitted to 2,268 individual bubble observations, several predictors take on only a small number of distinct values: the Morton number is defined by three continuous phase fluids, and the viscosity ratio is effectively defined by two organic phases crossed with three continuous phases. As a result, the effective degrees of freedom at the fluid system level are considerably lower than the observation count. Therefore, the reported p-values do not imply that the exponents are determined with the precision suggested by the standard errors alone. The near-zero viscosity ratio exponent ($\eta^{0.002}$, $p = 0.984$) should not be interpreted as evidence that the viscosity ratio is physically unimportant. The correlation was fitted using only two organic phase liquids (kerosene and sunflower oil), crossed with three continuous phases, giving six discrete (η, Mo) combinations in total. A power-law exponent describes a continuous trend, and six points spanning only two η levels are statistically insufficient to establish or rule out such a trend. The fitted exponent reflects the aggregate behavior across these six combinations rather than an independently resolved, continuous dependence on η. Extending the tested range to include additional organic phases at intermediate viscosities would be required before drawing a firm conclusion about the physical role of the viscosity ratio

Residual analysis across all *2,268* internal observations (Fig. 6 and Fig. 7) confirms that the absolute errors are centered on zero and show no systematic bias. Approximately 85% of the absolute error falls within ±*0.05*, and *98%* remains below ±*0.15* across the full range of predicted drag values (C_D, *calc = 0.10–2.50*). The uncoated bubble baselines exhibit the tightest clustering, coated-bubble experiments show slightly broader distributions with occasional positive outliers in the intermediate range, likely reflecting transient coating dynamics not captured by the time averaged coating fraction.

The normality of the per experiment C_D distribution was assessed with the Shapiro–Wilk test. Table 8 has therefore been extended to report the median and the *25th/75th* percentiles of C_D alongside the mean based error metrics (*RMSE, MAE, MAPE*), so that the central tendency reported for each experiment is not distorted by the observed skew.

4.3. Validation of the model against an external dataset

The unified model was validated against 25 independent external datasets comprising 2,910 bubble measurements across diverse fluids (Cioncolini & Magnini, 2025) including water, glycerol solutions, castor oil, mineral oil, mercury and *GaInSn*, and gas types such as air, N_2, *He*, CO_2 and *Ar*. Across these external benchmarks, the model demonstrated predictive fidelity, achieving mean prediction deviations of approximately 5 - 6% across all validation datasets, with complete statistics reported in Appendix A.3. For coated-bubble validation, 28 data points from Ji et al. and Karp et al. covering silicone-oil-coated bubbles in water at *Re* = 274–989 were tested. The balance of external evidence is uneven: of the 2,910 validation measurements, 2,882 correspond to uncoated bubble systems across diverse fluids and gases, and only 28 correspond to coated-bubble systems. Consequently, while the unified model's broad generality is rigorously established for uncoated bubble dynamics, its generalization to coated systems, which represent

Table 7. Statistical results from the combined model for uncoated and coated bubbles, where n is the number of points in the experiments, R^2, RMSE, MAE, and MAPE are the model results, *Re*max, *Re*min, *Mo*max, *Mo*min, *Eo*max, and *Eo*min are the maximum and minimum values of the respective dimensionless numbers for each experiment.

Experiment	N	R^2	RMSE	MAE	MAPE	*Re*max	*Re*min	*Mo*max	*Mo*min	*Eo*max	*Eo*min
Water_Kerosene	103	0.83	0.06	0.04	3.98 %	420.70	262.06	1.32×10^{-10}	5.02×10^{-11}	1.53	0.50
Water_Oil	61	0.97	0.09	0.08	9.01 %	521.76	326.65	3.82×10^{-10}	7.76×10^{-11}	2.67	0.69
Water_Air	656	0.98	0.08	0.08	2.59 %	926.33	210.38	2.57×10^{-11}	2.57×10^{-11}	2.20	0.28
Salt_Air	570	0.94	0.05	0.04	1.84 %	579.92	262.74	3.78×10^{-10}	3.78×10^{-10}	2.89	0.69
Salt_Kerosene	66	0.97	0.14	0.11	7.35 %	1131.45	207.05	1.44×10^{-9}	7.37×10^{-10}	18.50	0.84
Saltl_Oil	248	0.96	0.11	0.09	6.44 %	1876.88	231.42	3.44×10^{-9}	1.32×10^{-9}	49.58	1.40
Sugar_Kerosene	173	0.99	0.03	0.02	2.15 %	198.35	97.72	1.02×10^{-7}	5.90×10^{-8}	3.07	1.30
Sugar_Oil	219	0.99	0.02	0.02	1.74 %	275.34	140.10	2.81×10^{-7}	1.92×10^{-7}	7.09	2.70
Sugar_Air	172	1.00	0.05	0.05	0.96 %	99.70	56.16	2.40×10^{-8}	2.40×10^{-8}	0.85	0.53

Table 8. Statistical results. Median, Q25, and Q75 are the median and interquartile range of the observed drag coefficient per experiment; Skewness and Shapiro-Wilk p assess the normality of the underlying C_D distribution, with the Normality chek flag indicating whether the null hypothesis of normality is not rejected ($p > 0.05$).

Experiment	Median Cd	Q25 C_D	Q75 C_D	Skewness	Shapiro-Wilk p	Normality check
Water_Kerosene	1	0.95	1.07	2.28	5.59×10^{-10}	No
Water_Oil	1.225	1.008	1.3	-0.61	3.42×10^{-14}	No
Water_Air	0.8	0.69	1	0.49	1.16×10^{-13}	No
Salt_Air	0.73	0.67	0.79	0.28	5.21×10^{-03}	No
Salt_Kerosene	0.95	0.84	1.205	1.59	2.92×10^{-11}	No
Saltl_Oil	0.89	0.75	1.21	1.33	2.35×10^{-17}	No
Sugar_Kerosene	0.64	0.58	0.68	0.06	5.63×10^{-01}	Yes
Sugar_Oil	0.51	0.475	0.56	0.75	1.97×10^{-05}	No
Sugar_Air	0.87	0.83	0.942	-0.06	5.55×10^{-02}	Yes

the more novel contribution of this work. Expanded coated-bubble validation, covering a wider range of organic phases, coating fractions, and continuous-phase properties, is needed before the unified model can be considered fully validated for industrial coating conditions.

To situate the unified correlation within the existing literature, Table 9 presents a head-to-head predictive comparison against four published correlations applied to the same validation dataset. The Tomiyama et al. (1998) and Yan et al. (2017) correlations were evaluated across all 5,354 validation observations; both achieve moderate performance on uncoated bubble subsets but fail on coated conditions, yielding *MAE* of 0.380 and 0.238 and R^2 of 0.446 and 0.67, respectively, compared with *MAE* of 0.05 and R^2 of 0.97 for the present model. The Kawano and Hashimoto (1997) correlation was evaluated only on the

1,073 observations satisfying its stated $Re < 200$ restriction; even within this reduced range, it yields $R^2 = 0.04$ and $MAE = 0.3$, indicating that its low Re analytical form does not generalize well to the fluid diversity of the validation set. The Karp et al. (2021) correlation, evaluated on the 1,039 coated-bubble observations for which a base uncoat-bubble C_D could be estimated, yields $R^2 \approx 0.12$ and $MAE = 29.6$, reflecting the sensitivity of relative-correction formulations to errors in the required input drag coefficient. The models used are in Appendix A.2

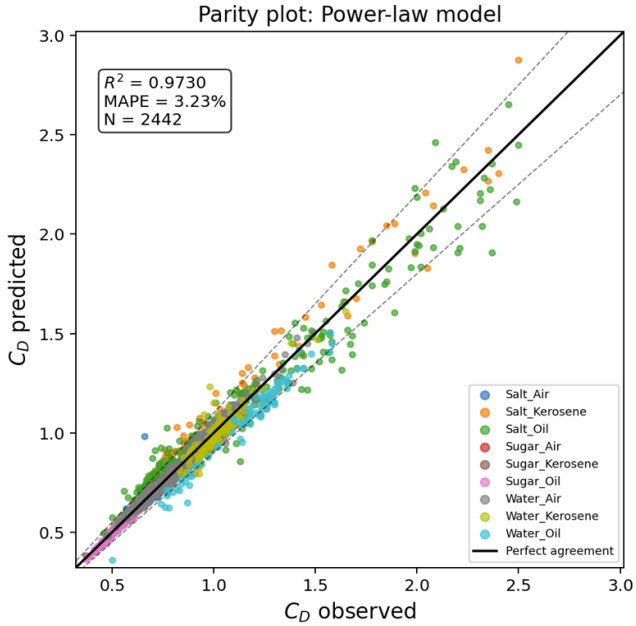

Fig. 6. Experimental drag coefficient and theoretical drag coefficient for all the measurements of the work, using the combined model, straight lines represent the interval of 10% and -10% of the observed drag coefficient

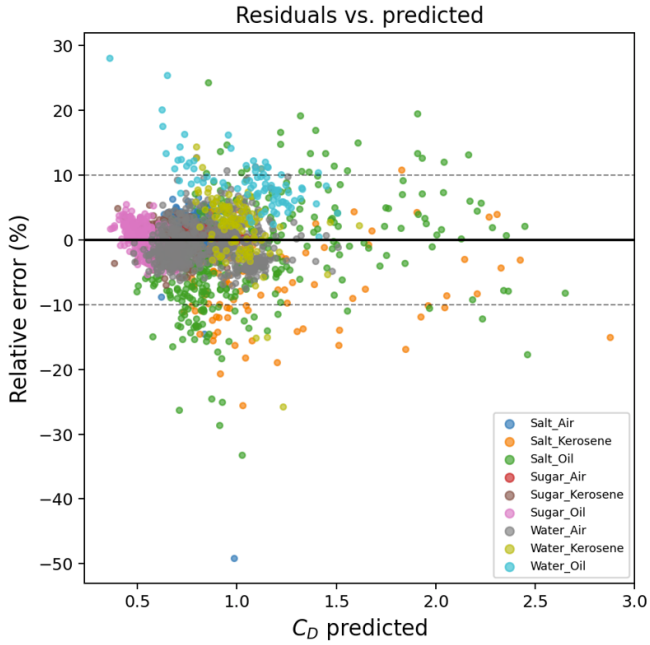

Fig. 7. Residuals for the drag coefficient calculated from the combined model. Absolute error calculated as $\frac{|CdCalc - CdExp|}{Cdexp}\%$

Table 9. Statistical results from the combined model for uncoated and coated bubbles, and other authors' models, where n is the number of points in the experiments, and R2, RMSE, MAE, and MAPE are the model results.

Model	N	R^2	RMSE	MAE	MAPE
Proposed model	5354	0.97	0.08	0.05	4.75%
Tomiyama(Tomiyama et al., 1998)	5354	0.46	0.55	0.38	79%
Yan(Yan et al., 2017)	5354	0.67	0.45	0.24	48%
Kawano(Kawano & Hashimoto, 1997)	1073	0.04	0.28	0.30	40%
Karp(Karp et al., 2021)	1039	0.12	49.82	29.60	72%

Residual analysis confirms unbiased predictions for $30 < Re < 1000$ and $0.1 < Eo < 10$, defining the model's reliable operating window. Outside these limits, errors grow systematically, reflecting the breakdown of the power law form near the Stokes transition ($Re < 30$) and under strong surface tension dominance ($Eo < 0.1$). Fig. 8 to Fig. 11 present the residual distributions and the absolute error histogram for the data set.

Prediction errors arise from physical phenomena absent from the quasi-steady axisymmetric formulation. R. Chen et al. (2026) showed that Marangoni stresses create spatially heterogeneous boundary conditions transitioning from free-slip to no-slip, promoting flow separation not captured by the model. Von Kameke et al. (2026) resolved three dimensional secondary vortex loops in ellipsoidal bubble wakes at $Re \sim 800$, with vorticity production exceeding clean sphere predictions by a factor of two. In coated bubbles, these unsteady wake phenomena, including lift forces, additional drag from vortex asymmetry, and periodic shedding, introduce time dependent lateral forcing that a quasi-steady model cannot represent, consistent with the increased scatter in C_D observed in the oscillatory trajectory regime.

Oscillatory trajectories introduce systematic scatter: when bubbles follow zigzag or helical paths, the measured vertical velocity underestimates true speed, producing a positive bias in C_D through the v_t^{-2} dependence in Equation 3. The acceptance criterion requiring a standard deviation below 10% of the mean velocity partially mitigates this effect. However, bubbles in the early stages of path instability may still pass this filter, consistent with the broader residual distributions observed in coated-bubble experiments. Karp et al. (2021) reported more scattered drag data for compound drops following oscillatory paths than for those with rectilinear trajectories, supporting this interpretation.

The model's reliable operating window is $30 < Re < 1000$ and $0.1 < Eo < 10$, within which absolute error is unbiased and randomly distributed. Below $Re = 30$, the power-law form fails to capture the steep C_D gradient near the Stokes transition. Below $Eo = 0.1$, strong surface-tension resistance places bubbles in a regime where small perturbations produce disproportionate changes in drag. Above $Re = 1000$ and $Eo = 10$, path instabilities, wake shedding, and bubble fragmentation violate the quasi-steady assumptions of the force balance. Within these boundaries, the unified model yields a mean absolute error of approximately 5 – 6%.

4.4. Importance of dimensionless numbers and coating fraction

The exponents are consistent across all three models, suggesting that the dominant hydrodynamic balances are preserved between uncoated and coated regimes. Re exponents range from -2.02 to -2.08 across the three correlations, reflecting the viscous to inertial transition in the intermediate regime; the multivariate value of approximately -2.0 should not be directly compared with single-variable scalings, such as the Stokes limit. The Eo exponent is positive across all models, suggesting that wake-related pressure effects may contribute to drag beyond the projected-area increase alone. However, the two contributions cannot be separated from the present data.

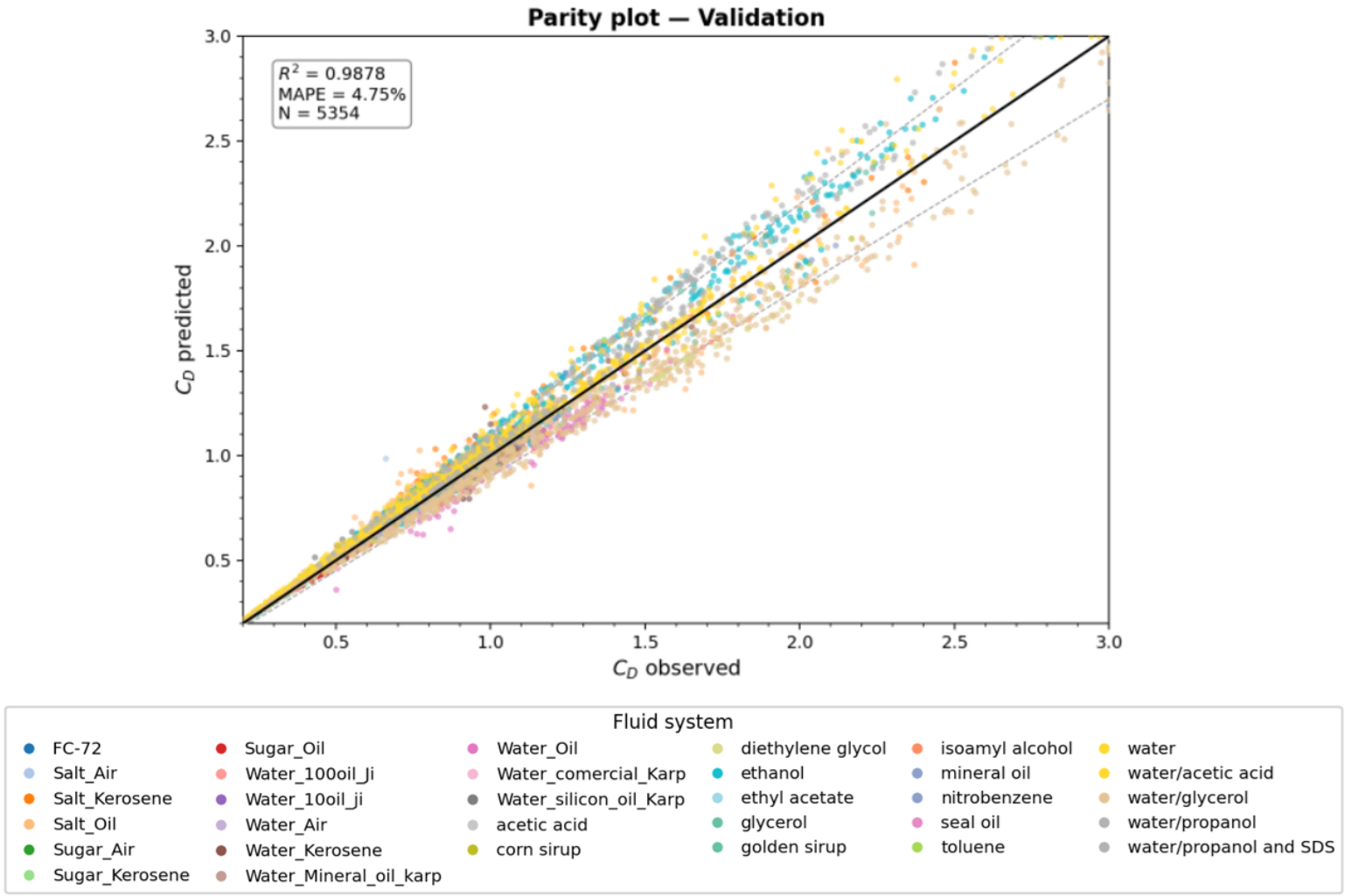

Fig. 8. Experimental and theoretical drag coefficients for all measurements in this work, using the combined model. Straight lines represent the 10% and -10% intervals of the observed drag coefficient.

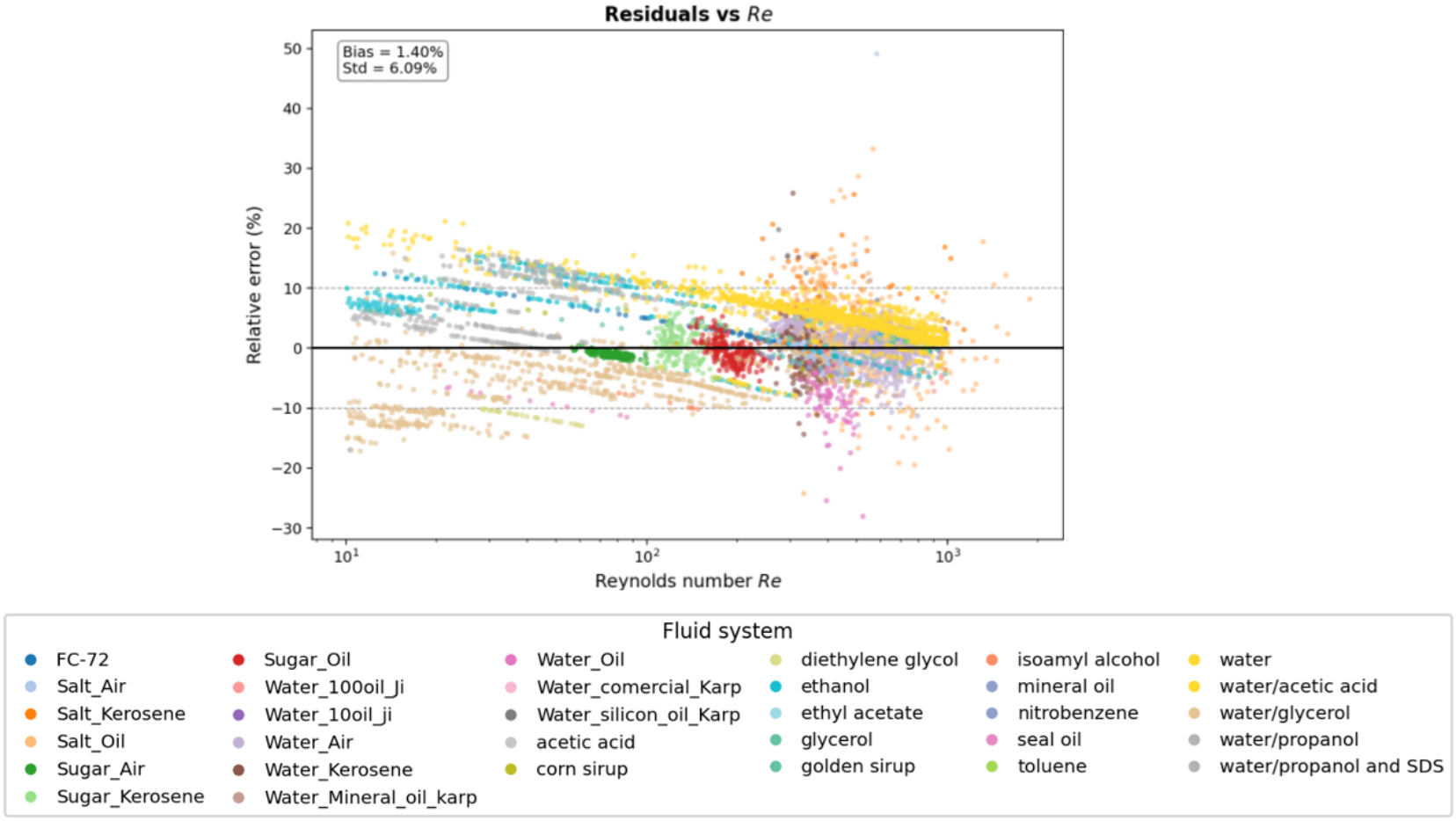

Fig. 9. Error values for the Reynolds number from validation data using the unified model. Absolute error calculated as $\frac{|C_D Calc - C_D Exp|}{C_D exp}$

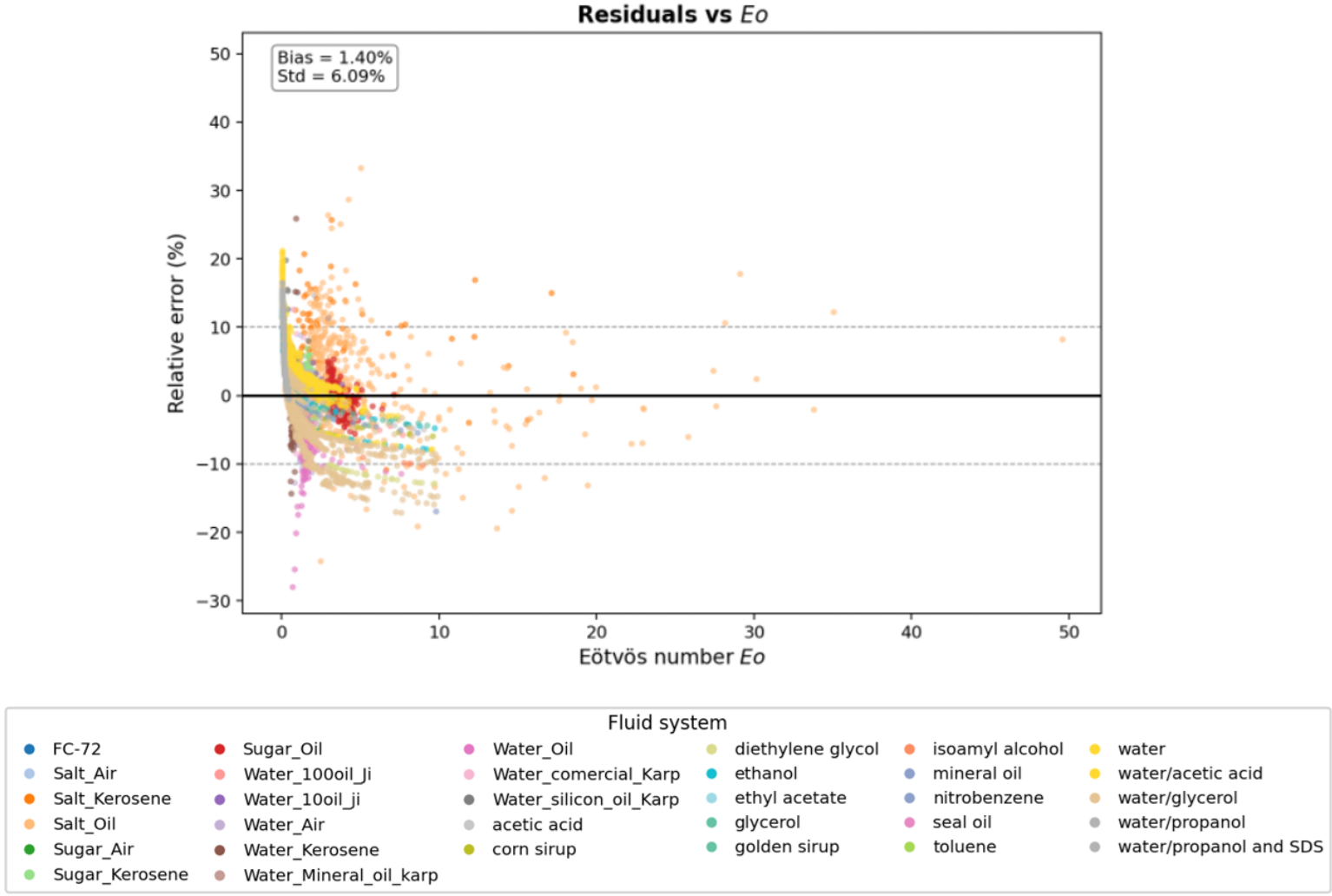

Fig. 10. Error values for the Eötvös number from validation data using the unified model. Absolute error calculated as $\frac{|C_D Calc - C_D Exp|}{C_D exp}$

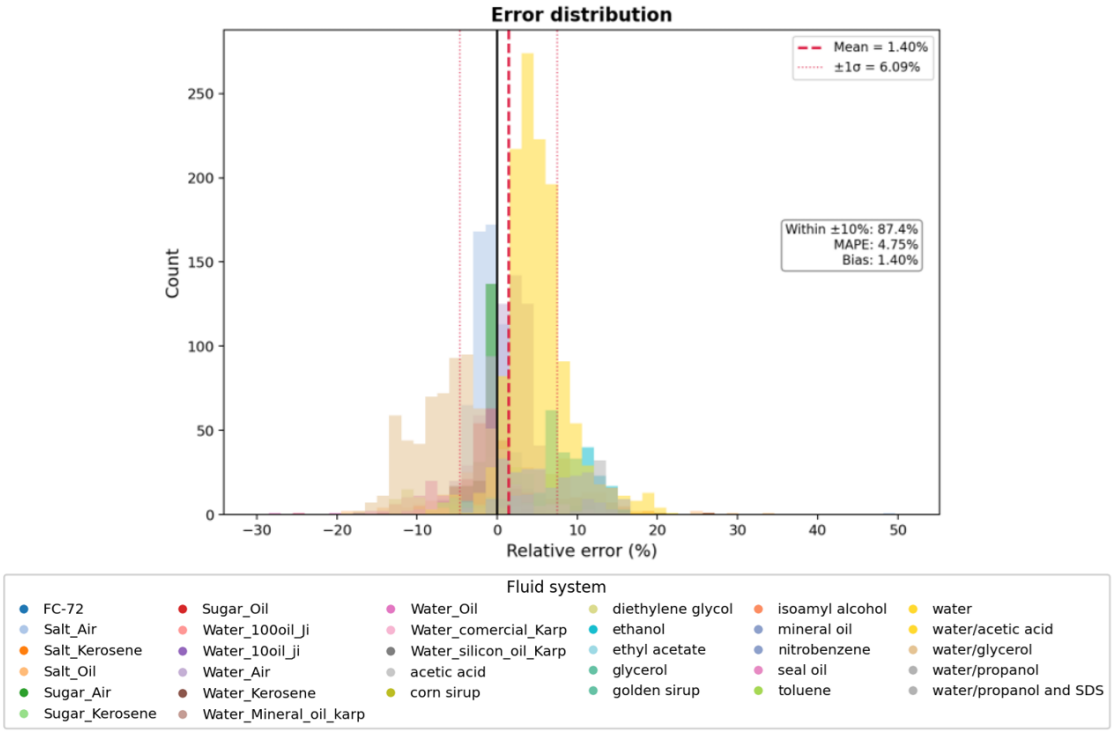

Fig. 11. Error histogram for the proposed model across all data used in this research and validation data

All three models yield *Mo* exponents of approximately *-0.52*, indicating that higher *Mo* fluids produce lower C_D at fixed *Re* and *Eo*. This is consistent with viscosity damping wake instabilities and delayed vortex shedding, though direct wake measurements would be required to confirm this mechanism. The coating fraction exponent is small and negative, with a tenfold increase in oil fraction producing an estimated 18% reduction in C_D, partially absorbed into *Eo* and *Mo* through the apparent density and interfacial tension. The viscosity ratio η contributes negligibly to prediction in both the coated and unified models within the present experimental range. This does not imply that η is physically irrelevant across all conditions; rather, the viscosity ratio was explored using only two organic phases, kerosene (η = *0.34–1.99*) and sunflower oil (η = *9.83–58*), which is statistically insufficient to establish or rule out a continuous power law trend (Section 4.2). The near-zero exponent should therefore be interpreted as evidence that η is unresolved within the tested window $0.34 \leq \eta \leq 58$, not as evidence that the viscosity ratio is irrelevant in general. Whether a threshold exists above which η becomes a primary control parameter, particularly for $\eta > 100$ or for organic phases with substantially different interfacial rheology, cannot be determined from the current data. The regression exponents provide a coherent physical picture: *Re* and *Eo* govern the viscous inertial and deformation driven contributions, respectively, with exponents invariant between uncoated and coated conditions.

4.5. Implications for drift-flux and multiphase models

The unified correlation provides a drag closure for drift-flux and multiphase flow models that include coated bubble populations. In flotation columns and solvent extraction contactors, it replaces the uncoated bubble drag assumption with a formulation that explicitly accounts for oil coating, coating fraction, and continuous-phase properties. As shown by Leiva et al. (2024), systematic errors in C_D propagate directly into gas holdup and bubble-size estimates; the unified model reduces these

errors without requiring a priori knowledge of the base drag coefficient. The tested *Re*–*Eo* window ($30 < Re < 1000$ and $0.1 < Eo < 10$) overlaps the operating range of many industrial flotation columns and laboratory solvent extraction contactors with bubble diameters in the 1–5 mm range; however, real flotation pulps and extraction systems introduce surfactants (frothers, collectors), phase impurities, and viscosity ratios that may extend beyond the conditions tested here, and the correlation's applicability to those systems should be confirmed with dedicated validation rather than assumed from the present dataset.

Existing drift-flux closures based on uncoated bubble correlations systematically underpredict C_D for coated populations, overpredicting rise velocity and underpredicting gas holdup. The unified correlation corrects this bias while remaining consistent with uncoated bubble behavior when no coating is present. For flotation column design, improved holdup predictions are expected in systems with organic reagents or collector-coated bubbles. In coated bubble solvent extraction columns, accurate drag prediction is a prerequisite for reliable scale up, as errors in rise velocity propagate into extraction kinetics and column height requirements.

Accurate drag modeling also enables estimation of the specific interfacial area available for mass transfer, since the interfacial area per unit volume depends on both bubble diameter and gas holdup, both of which are accounted for in the drag closure. In hollow drop solvent extraction systems, the unified correlation provides the hydrodynamic link between laboratory scale drag measurements and column mass transfer models, opening a path toward rational scale up from bench to industrial scale. Additionally, the statistical significance of individual exponents, particularly for η and φ_{air}, should be treated with caution. These predictors are defined by only a small number of experimental levels, and their fitted exponents reflect the aggregate behavior across the tested fluid combinations rather than independently resolved effects.

The correlations were developed under quiescent conditions; application under circulating or turbulent flow requires verification of the slip velocity closure, as possible wake modification and bubble-bubble interactions are absent from single bubble experiments. The force balance assumes quasi steady, axisymmetric flow around an oblate spheroid, an assumption that breaks down near the upper *Re* limit. The model also assumes a continuous, concentric oil shell of uniform thickness. In contrast, real coated bubbles may have eccentric configurations, partial coatings, or dynamic oil redistribution during rise, none of which are captured by the time averaged coating fraction.

The continuous phases examined here (tap water, NaCl solution, sucrose solution) are frother free and contain only trace, uncontrolled surface-active contaminants. Frother addition, as used deliberately in industrial flotation to control bubble size and film drainage, further modifies interfacial mobility beyond the baseline contamination already discussed in the Fluid Properties section, typically producing smaller bubbles with a more rigid interface at a given gas rate (Navarra et al., 2008). Because no frother dosed condition was tested in this work, extension of the present correlation to frother active flotation pulp remains an open question that should be addressed by dedicated experiments spanning representative frother types and concentrations.

Predictive accuracy degrades outside the range $30 < Re < 1000$ and $0.1 < Eo < 10$, where the power law form fails near the Stokes transition and under strong surface-tension dominance. The viscosity ratio range (0.34 *to* 58) does not extend to very heavy oils ($\eta > 100$), and the coating fraction is bound by image analysis acceptance criteria ($0.07 < \varphi_{air} < 0.93$). The correlation was developed for kerosene and sunflower oil. At the same time, external validation against silicone oil data confirms reasonable generalizability; however, coating materials with substantially different interfacial rheology or non-Newtonian behavior may not be adequately described.

As noted in Section 4.3, external validation of the coated-bubble branch rests on a small, imbalanced sample, 28 measurements against 2,882 for the uncoated branch, and its predictions should be treated as preliminary until a larger, independent coated-bubble dataset becomes available.

5. Conclusions

This work presents a systematic experimental investigation and unified empirical correlation for the drag coefficient of uncoated and oil coated bubbles across a deliberately constructed matrix of three continuous phases and two organic phases, spanning viscosity ratios from *0.34 to 58* and covering *2,268* individual bubble observations in the intermediate Reynolds number regime.

The experimental results establish that drag modification by oil coating is not universally monotonic but depends critically on the viscosity ratio between the coating and the continuous phase. In water and salt systems, coated bubbles exhibit systematically higher drag than uncoated bubbles, consistent with progressive interfacial immobilization by the oil shell. In the sucrose system, where the coating is less viscous than the continuous phase, coated bubbles exhibit lower drag than the uncoated baseline, providing direct empirical evidence of a viscosity ratio driven drag reversal not previously documented across multiple fluid systems within a single experimental program. Across all systems, the difference in drag between the two organic phases is modest, suggesting that *Re* and *Eo* are the dominant control parameters, with the viscosity ratio acting as a secondary modifier. This conclusion is bounded by the tested viscosity ratio range (*0.34 to 58*) and the limited number of organic phases examined; extension to higher η values is required to determine whether this secondary status persists.

Three empirical power law correlations were developed: an uncoated bubble model, a coated bubble model, and a unified model combining both regimes. The exponents for *Re*, *Eo*, and *Mo* are consistent across all three models, indicating that the fundamental hydrodynamic scaling is preserved in both the uncoated and coated regimes. The primary effect of the oil coating arises from a shift in the prefactor rather than a change in the scaling exponents, consistent with progressive interfacial immobilization without altering the underlying drag mechanisms. External validation across 25 independent datasets confirms the generalizability of the unified correlation for uncoated bubble systems; validation of the coated bubble branch remains preliminary (Section 4.3) and should be extended with a larger, independent coated bubble dataset in future work.

The unified correlation provides a practical drag closure for drift-flux and multiphase flow models applied to flotation columns, solvent extraction contactors, and bubble column reactors that contain coated bubble populations. It reduces to a three parameter uncoated bubble model when no coating is present, providing a seamless framework across both regimes within a single equation. Future work should extend the parameter range, incorporate time resolved measurements of coating fraction, and validate the correlation under realistic operating flow conditions to enable direct implementation in industrial process models. The correlation was developed and validated under quiescent, single bubble conditions with a continuous and approximately concentric oil shell. Its application to industrial systems involving turbulence, bubble interactions, oscillatory rise paths, partial coatings, or dynamic oil redistribution lies outside the scope of its current validation and should be approached with caution.

6. Future work and perspectives

Extending the experimental matrix to $Re > 1000$ and $Eo > 10$ would cover the bubble cap and churn turbulent regimes relevant to large scale contactors. Systematic variation toward $\eta > 100$ would clarify whether the near zero viscosity ratio exponent persists at extreme values or whether a threshold exists above which η becomes a primary control parameter. Coupled CFD–PIV validation, using particle image velocimetry measurements to benchmark numerical simulations, would resolve the wake stabilization mechanisms inferred from regression exponents and separate viscous from pressure drag contributions.

Appendices A

A.1 Experimental data from other sources

The experimental bubble-rise database follows the same structure as (Cioncolini & Magnini, 2025), with references for each publication.

Experiment number	Author(s)	Primary Liquid(s)	Gas
10	Tomiyama et al.(Tomiyama et al., 2002)	Water	Air
11	Aoyama et al.(Aoyama et al., 2016)	Water/Glycerol	Air
15	Duineveld(P. Duineveld, 1996)	Water	Air
16	Haberman(Haberman & Morton, 1953) and Morton	Water, Water/Glim, Varsol, Mineral Oil	Air
17	Rosenberg(Rosenberg B, 1950)	Water	Air
18	Kojima et al.(Kojima et al., 1968)	Castor Oil, Glycerol, Corn Syrup	Air
14	Liu et al.(Liu et al., 2016)	Water, Water/Glycerol	Air
19	Redfield and Houghton(Redfield & Houghton, 1965)	Water, Water/Sugar	CO_2
12	Parkinson et al.(Parkinson et al., 2008)	Water	Air, N_2, He, CO_2
20	Davenport et al.(Davenport et al., 1967)	Water, Ethyl Alcohol, Water/PVA	Air, N_2
22	Tadaki and Maeda(Tadaki & Maeda, 1961)	Ethyl Acetate, Toluene, Water/Salt, Water/Ethanol, Ethanol, Nitrobenzene, Water/Acetic Acid, Isoamyl Alcohol, Water/Glycerol	Air
24	Maxworthy et al.(Maxworthy et al., 1996)	Water, Water/Glycerol	Air
23	Akehata et al.(Akehata et al., 1967)	Water, Water/Glycerol, Ethyl Acetate, Acetic Acid	Air
25	O'Brien and Gosline(O'brien & Gosline, 1935)	Water, Livestock Oil, Mineral Oil	Air
26	Calderbank and Lochiel(Calderbank & Lochiel, 1964)	Water	CO_2
27	Bryn(Bryn, 1949)	Water	Air
28	Cai et al.(Cai et al., 2010)	Water, Water/Glycerol, Glycerol	Air
21	Angelino(Angelino, 1966)	Glycerol, Compressor Oil, DP/TP Glycol	Air
29	Garner and Hammerton(Garner & Hammerton, 1954)	Water	Air, Ethylene

Experiment number	Author(s)	Primary Liquid(s)	Gas
30	Baird and Davidson(Baird & Davidson, 1962)	Water	CO_2
31	Davies and Taylor(Davies & Taylor, 1988)	Nitrobenzene	Air
32	Miyagi(Miyagi, 1925)	Water	Air
33	Aoyama et al.(Aoyama et al., 2018)	Water/Glycerol	Air
34	Bachhuber (Bachhuber & Sanford, 1974)and Sanford	Water	Air
35	Sanada et al.(Sanada et al., 2008)	Water	N_2
36	Hnat and Buckmaster(Hnat & Buckmaster, 1976)	Mineral Oil	Air
37	Krishna et al.(Krishna et al., 1999)	Water, Tellus Oil	Air
39	Mori et al(Mori et al., 1977).	Mercury	N_2
41	Schwerdtfeger(Schwerdtfeger, 1968)	Water, Mercury	Air, Ar
42	Bhaga and Weber(Bhaga & Weber, 1981)	Water/Sugar	Air
44	Wang et al.(Z. H. Wang et al., 2017)	Water, GaInSn	Ar
43	Zhang et al.(Zhang et al., 2005)	Water, GaInSn	Ar
45	Uno and Kintner(Uno & Kintner, 1956)	Water, Water/Glycerol, Diethylene Glycol	Air
46	Calderbank et al.(Calderbank et al., 1970)	Water, Water/Glycerol	CO_2
47	Strumpf (Strumpf, 2017)	GaInSn	Ar
48,49	Ji et al(Ji et al., 2022)	Water, Silicon oil and Air	Air Coated
50,51,52	Karp et al.(Karp et al., 2021)	Water, Silicon oil and air	Air Coated

A.2 Terminal velocity and Drag models

Terminal velocity models are used in Fig. 4 and Fig. 3

Author	Correlation	Remarks
Mendelson(Mendelson, 1967)	$\sqrt{\frac{2\sigma}{\rho_l d}+\frac{gd}{2}}$	Intermediate to large bubbles

Author	Correlation	Remarks
	$\frac{1}{\sqrt{\frac{1}{v_{t1}^2}+\frac{1}{v_{t2}^2}}}$	
Baz-Rodriguez(S. Baz-Rodríguez et al., 2012)	$v_{t,pot}=\frac{1}{36}\frac{\Delta\rho g d^2}{\mu_l}$ $v_{t1}=v_{t,pot}\left[1+0.73667\frac{(gd)^{1/2}}{v_{t,pot}}\right]^{1/2}$ $v_{t2}=\sqrt{\frac{3\sigma}{\rho_l d}+\frac{gd\Delta\rho}{2\rho_l}}$ $v_t=(v_{b1}^{-n}+v_{b2}^{-n})^{-1/n}$	Pure liquids and a wide range of Reynolds numbers
Fan and Tsuchiya(Tsuchiya et al., 2013)	$v_{b1}=\frac{\rho_l g d^2}{K_b\mu_l}$ $v_{b2}=\sqrt{\frac{2c\sigma}{\rho_l d}+\frac{gd}{2}}$ $K_b=max(12,K_{b0}Mo^{-n})$	Where K_{b0},c and n are constant for different fluids.

Author	Correlation	Remarks
Tomiyama (Tomiyama et al., 1998)	$C_D=max\left\{\frac{24}{Re}(1+0.15*Re^{0.687}),\frac{8}{3}\frac{Eo}{Eo+4}\right\}$	Contaminated bubbles
Yan(Yan et al., 2017)	$C_D=max\left\{min\left(\frac{24}{Re}(1+0.15*Re^{0.687}),\frac{8}{3}\frac{Eo}{Eo+4}\right),\frac{24}{Re}(1+0.15*Re^{0.687})*\frac{Re^{0.55}*Eo^{0.95}*We^{-1.1}}{12.6}\right\}$	Air bubbles
Kawano(Kawano & Hashimoto, 1997)	$C_D=\frac{0.195}{2.25^{1.9}}*B^{2*1.9+1}\left\{1+\frac{9.06}{\sqrt{Re}}(\frac{1.5}{B})^{1.9}\right\}^2$	For B=1 for bubbles and B=1.5 for drops
Karp(Karp et al., 2021)	$C_{D_d}^{\ s}=\frac{24}{Re}(1+0.15*Re^{0.687})$ $C_{D_d}^{\ b}=\frac{16}{Re}*(\frac{16+3.315Re^{1/2}+3*Re}{16+3.315Re^{1/2}+Re})$ $C_{D_d}^{\ d}=\frac{C_{D_d}^{\ b}+\eta*C_{D_d}^{\ s}}{1+\eta}$ $C_D=C_D*\left[1-P*(\frac{db}{dcb})^3\right]$	Where P=0.43*$\eta^{0.58}$ db=bubble diameter dcb coated bubble diameter

A.3 Summary of statistics for the drag coefficient model

Exp.	n	R^2	RMSE	MAE	Re max	Re min	Mo max	Mo min	Eo max	Eo min
0	5354	0.95	0.23	0.12	1876.88	10.03	1.87×10^{-2}	4.40×10^{-13}	49.58	0.01
1	109	0.83	0.06	0.04	420.70	262.06	1.32×10^{-10}	5.02×10^{-11}	1.53	0.50
2	84	0.97	0.09	0.08	521.76	326.65	3.82×10^{-10}	7.76×10^{-11}	2.67	0.69
3	659	0.98	0.08	0.08	926.33	210.38	2.57×10^{-11}	2.57×10^{-11}	2.20	0.28
4	572	0.94	0.05	0.04	579.92	262.74	3.78×10^{-10}	3.78×10^{-10}	2.89	0.69
5	107	0.97	0.14	0.11	1131.45	207.05	1.44×10^{-9}	7.37×10^{-10}	18.50	0.84
6	347	0.96	0.11	0.09	1876.88	231.42	3.44×10^{-9}	1.32×10^{-9}	49.58	1.40
7	173	0.99	0.03	0.02	198.35	97.72	1.02×10^{-7}	5.90×10^{-8}	3.07	1.30
8	219	0.99	0.02	0.02	275.34	140.10	2.81×10^{-7}	1.92×10^{-7}	7.09	2.70
9	172	1.00	0.05	0.05	99.70	56.16	2.40×10^{-8}	2.40×10^{-8}	0.85	0.53
10	1278	0.96	0.24	0.13	998.18	10.15	3.12×10^{-10}	4.40×10^{-13}	7.36	0.01
11	691	0.96	0.28	0.16	956.56	10.03	4.93×10^{-3}	8.02×10^{-11}	9.90	0.03
16	33	0.96	0.24	0.14	984.22	16.50	4.44×10^{-10}	4.44×10^{-10}	9.23	0.04
17	16	0.95	0.30	0.15	462.13	12.77	2.40×10^{-9}	2.40×10^{-9}	5.51	0.05
18	10	1.00	0.07	0.06	827.02	57.70	8.83×10^{-11}	8.83×10^{-11}	3.04	0.06
14	3	1.00	0.39	0.37	18.40	14.16	2.10×10^{-3}	1.43×10^{-4}	7.67	2.96
25	12	1.00	0.09	0.09	996.90	186.54	3.94×10^{-11}	3.27×10^{-11}	2.51	0.25
26	6	1.00	0.09	0.09	858.32	660.00	7.46×10^{-11}	7.46×10^{-11}	2.58	1.13
27	13	1.00	0.10	0.09	920.20	592.37	8.04×10^{-11}	5.80×10^{-11}	3.26	0.98
28	271	0.96	0.51	0.37	862.95	10.03	4.43×10^{-8}	2.95×10^{-11}	9.71	0.03
21	13	0.94	0.17	0.09	538.51	18.96	3.94×10^{-9}	1.75×10^{-9}	9.56	0.07
29	15	1.00	0.02	0.02	555.79	188.63	2.68×10^{-9}	2.68×10^{-9}	8.64	0.59
30	23	1.00	0.04	0.03	311.37	111.36	4.15×10^{-8}	4.15×10^{-8}	9.52	0.91
31	13	0.93	0.11	0.07	147.50	20.47	8.05×10^{-7}	8.05×10^{-7}	8.97	0.56
32	7	1.00	0.06	0.06	802.87	257.53	1.02×10^{-9}	1.02×10^{-9}	9.03	1.04
34	11	0.73	0.12	0.10	85.60	21.58	6.28×10^{-6}	6.28×10^{-6}	7.58	1.10
39	34	0.84	0.07	0.06	60.90	28.27	2.90×10^{-5}	2.90×10^{-5}	9.71	3.03
44	208	0.98	0.48	0.41	133.70	10.52	4.26×10^{-8}	2.28×10^{-11}	0.28	0.03
43	3	0.99	0.98	0.98	12.45	11.55	1.66×10^{-8}	1.66×10^{-8}	0.10	0.09
46	100	0.99	0.28	0.21	83.63	15.65	4.62×10^{-8}	2.73×10^{-11}	0.49	0.03
47	114	0.95	0.11	0.06	671.32	13.37	7.59×10^{-10}	7.59×10^{-10}	4.59	0.03
48	7	1.00	0.11	0.11	988.56	937.90	8.99×10^{-11}	3.88×10^{-11}	3.82	1.99

Exp.	n	R^2	RMSE	MAE	Re max	Re min	Mo max	Mo min	Eo max	Eo min
49	6	0.99	0.06	0.06	956.79	889.05	7.21×10^{-10}	3.20×10^{-10}	7.66	4.07
50	8	0.97	0.07	0.06	583.39	273.96	9.78×10^{-11}	2.29×10^{-11}	1.66	0.24
51	7	0.92	0.05	0.05	616.98	425.77	3.11×10^{-10}	1.17×10^{-10}	2.22	0.70
52	7	0.91	0.03	0.02	661.71	386.03	2.40×10^{-9}	1.20×10^{-9}	4.70	1.37

References

ACUÑA, C. A., RADMAN, J., FINCH, J. A. 2008. *Measurement of flow visualized on surface of bubble blown in air.* Colloids and Surfaces A: Physicochemical and Engineering Aspects, 330(2–3), 112–115.

ACUÑA PÉREZ, C. ABRAHAM. 2010. *Measurement techniques to characterize bubble motion in swarms [Book].* McGill University.

AKEHATA, T., SHIRAI, T., KUBOTA, M. 1967. *The behavior of single air bubbles in liquids of small viscosity.* Kagaku Kōgaku, 31(11), 1074–1080, a1.

ANGELINO, H. 1966. *Hydrodynamique des grosses bulles dans les liquides visqueux.* Chem. Eng. Sci, 21(6–7), 541–550.

AOYAMA, S., HAYASHI, K., HOSOKAWA, S., TOMIYAMA, A. 2016. *Shapes of ellipsoidal bubbles in infinite stagnant liquids.* Int. J. Multiph. Flow, 79, 23–30.

AOYAMA, S., HAYASHI, K., HOSOKAWA, S., TOMIYAMA, A. 2018. *Shapes of single bubbles in infinite stagnant liquids contaminated with surfactant.* Exp. Therm. Fluid Sci, 96, 460–469.

AYOGLU, O., HOANG, D. H., SINCHE-GONZALEZ, M., HASSANZADEH, A., RUDOLPH, M. 2025. *Investigating hydrodynamics of a laboratory-scale ImhoflotTM V-cell in recovering ultrafine magnesite from a dolomite-rich tailing.* Minerals Engineering, 232, 109548.

AZGOMI, F., GOMEZ, C. O., FINCH, J. A. 2007. *Correspondence of gas holdup and bubble size in presence of different frothers.* International Journal of Mineral Processing, 83(1–2), 1–11.

BACHHUBER, C., SANFORD, C. 1974. *The rise of small bubbles in water.* J. Appl. Phys, 45(6), 2567–2569.

BAIRD, M. H. I., DAVIDSON, J. F. 1962. *Gas absorption by large rising bubbles.* Chem. Eng. Sci, 17(2), 87–93.

BESAGNI, G., INZOLI, F., ZIEGENHEIN, T. 2018. *Two-Phase Bubble Columns: A Comprehensive Review.* ChemEngineering 2018, 2, 2(2), 1–80.

BHAGA, D., WEBER, M. E. 1981. *Bubbles in viscous liquids: shapes, wakes and velocities.* Journal of Fluid Mechanics, 105, 61–85.

BRYN, T. 1949. *Speed of rise of air bubbles in liquids.*

CAI, Z., BAO, Y., GAO, Z. 2010. *Hydrodynamic behavior of a single bubble rising in viscous liquids.* Chin. J. Chem. Eng, 18(6), 923–930.

CALDERBANK, P. H., JOHNSON, D. S. L., LOUDON, J. 1970. *Mechanics and mass transfer of single bubbles in free rise through some Newtonian and non-Newtonian liquids.* Chem. Eng. Sci, 25(2), 235–256.

CALDERBANK, P. H., LOCHIEL, A. C. 1964. *Mass transfer coefficients, velocities and shapes of carbon dioxide bubbles in free rise through distilled water.* Chem. Eng. Sci, 19(7), 485–503.

CHEN, J., HAYASHI, K., HOSOKAWA, S., TOMIYAMA, A. 2019. *DRAG CORRELATIONS OF ELLIPSOIDAL BUBBLES IN CLEAN AND FULLY CONTAMINATED SYSTEMS.* Multiphase Science and Technology, 31(3), 215–234.

CHEN, R., LIN, B., ZHANG, B., LI, X., YAN, X., ZHANG, H.c WANG, H. 2026. *Investigation of flow characteristics of the bubble surface in a flowing MIBC solution.* Separation and Purification Technology, 395.

CIONCOLINI, A., MAGNINI, M. 2025. *Solitary bubbles rising in quiescent liquids: A critical assessment of experimental data and high-fidelity numerical simulations, and performance evaluation of selected prediction methods.* In Physics of Fluids (Vol. 37, Number 2). American Institute of Physics.

CLIFT, R. ., GRACE, J. R. ., WEBER, M. E. . 2005. *Bubbles, drops, and particles.* Dover Publications.

DAVENPORT, W. G., RICHARDSON, F. D., BRADSHAW, A. V. 1967. *Spherical cap bubbles in low density liquids.* Chem. Eng. Sci, 22(9), 1221–1235.

DAVIES, R. M., TAYLOR, S. G. 1988. *The mechanics of large bubbles rising through extended liquids and through liquids in tubes.* In Dynamics of Curved Fronts (pp. 377–392). Elsevier.

DUINEVELD, P. 1996. *The rise velocity and shape of bubbles in pure water at high Reynolds number.* Int. J. Multiph. Flow, 22, 127.

DUINEVELD, P. C. 1995. *The rise velocity and shape of bubbles in pure water at high Reynolds number.* Journal of Fluid Mechanics, 292, 325–332.

GARNER, F. H., HAMMERTON, D. 1954. *Circulation inside gas bubbles.* Chem. Eng. Sci, 3(1), 1–11.

GOMEZ, C., ACUÑA, C., FINCH, J., PELTON, R. 2001. *Aerosol-enhanced flotation deinking of recycled paper: Silicone oil offers an effective way of forming a layer on the bubble surface.* PULP & PAPER-CANADA, (102), 28–30.

HABERMAN, W. L., MORTON, R. K. 1953. *An experimental investigation of the drag and shape of air bubbles rising in various liquids.* [David W. Taylor Model Basin],.

HADAMARD, J. 1911. *Mouvement permanent lent d'une sphere liquid et visqueuse dans un liquid visqueux.* (No Title), 152, 1735.

HAYAKAWA, T., SHIGETA, M. 1974. *TERMINAL VELOCITY OF TWO-PHASE DROPLET.* JOURNAL OF CHEMICAL ENGINEERING OF JAPAN, 7(2), 140–142.

HERRADA, M. A., EGGERS, J. G. 2023. *Path instability of an air bubble rising in water.* Proceedings of the National Academy of Sciences, 120(4).

HNAT, J. G., BUCKMASTER, J. D. 1976. *Spherical cap bubbles and skirt formation.* Phys. Fluids, 19(2), 182–194.

JI, B., HONG, L., KIM, J. T., CHAMORRO, L. P., FENG, J. 2022. *Dynamics of an oil-coated bubble rising in a quiescent water medium.* Physical Review Fluids, 7(3).

JI, B., YANG, Z., FENG, J. 2021. *Oil-coated bubble formation from submerged coaxial orifices.* Physical Review Fluids, 6(3).

JOHNSON, R. E. 1981. *Stokes flow past a sphere coated with a thin fluid film.* Journal of Fluid Mechanics, 110, 217–238.

JOHNSON, R. E., SADHAL, S. S. 1983. *Stokes flow past bubbles and drops partially coated with thin films.* Part 2. Thin films with internal circulation – a perturbation solution. Journal of Fluid Mechanics, 132, 295–318.

JOHNSON, R. E., SADHAL, S. S. 1985. *Fluid Mechanics of Compound Multiphase Drops and Bubbles.* Annual Review of Fluid Mechanics, 17(1), 289–320.

KAMEKE, A. V., UPHOFF, R., STEUWE, E., NISSEN, J. H., HOFFMANN, M., SCHLÜTER, M., KEXEL, F. 2026. *Experimental analysis of time resolved three-dimensional velocity and vorticity fields behind single rising bubbles using Lagrangian particle tracking velocimetry.* Chemical Engineering Science, 326, 123403.

KARP, J. R., MANCILLA, E., DA SILVA, F. S., LEGENDRE, D., ZENIT, R., MORALES, R. E. M. 2021. *The dynamics of compound drops at high Reynolds numbers: Drag, shape, and trajectory.* International Journal of Multiphase Flow, 142, 103699.

KAWANO, S., HASHIMOTO, H. 1997. *A Numerical Study on Motion of a Sphere Coated With a Thin Liquid Film at Intermediate Reynolds Numbers.* Journal of Fluids Engineering, 119(2), 397–403.

KOJIMA, E., AKEHATA, T., SHIRAI, T. 1968. *Rising velocity and shape of single air bubbles in highly viscous liquids.* J. Chem. Eng. Japan, 1(1), 45–50.

KRISHNA, R., URSEANU, M. I., VAN BATEN, J. M., ELLENBERGER, J. 1999. *Wall effects on the rise of single gas bubbles in liquids.* Int. Commun. Heat Mass Transf, 26(6), 781–790.

LEE, J., PARK, H. 2017. *Wake structures behind an oscillating bubble rising close to a vertical wall.* International Journal of Multiphase Flow, 91, 225–242.

LEGENDRE, D., ZENIT, R., VELEZ-CORDERO, J. R. 2012. *On the deformation of gas bubbles in liquids.* Physics of Fluids, 24(4).

LEIVA, C., ACUÑA, C., LUUKKANEN, S., CRUZ, C. 2024. *Enhancing bubble bize prediction in flotation processes: a drift flux model accounting for frother type.* Physicochemical Problems of Mineral Processing.

LIU, L., YAN, H., ZHAO, G., ZHUANG, J. 2016. *Experimental studies on the terminal velocity of air bubbles in water and glycerol aqueous solution.* Exp. Therm. Fluid Sci, 78, 254–265.

MASLIYAH, J. H. 1979. *Hindered settling in a multi-species particle system.* Chemical Engineering Science, 34(9), 1166–1168.

MAXWORTHY, T., GNANN, C., KÜRTEN, M., DURST, F. 1996. *Experiments on the rise of air bubbles in clean viscous liquids.* J. Fluid Mech, 321(1), 421–441.

MENDELSON, H. D. 1967. *The prediction of bubble terminal velocities from wave theory.* AIChE Journal, 13(2), 250–253.

MIYAGI, O. 1925. *The motion of an air bubble rising in water.* J. Soc. Mech. Eng, 28(95), 97–128.

MORI, Y., HIJIKATA, K., KURIYAMA, I. 1977. *Experimental study of bubble motion in mercury with and without a magnetic field.* J. Heat Transfer, 99(3), 404–410.

NAVARRA, A., ACUÑA, C., FINCH, J. A. 2008. *Impact of frother on the terminal velocity of small bubbles.* International Journal of Mineral Processing, 91, 68–73.

O'BRIEN, M. P., GOSLINE, J. E. 1935. *Velocity of large bubbles in vertical tubes.* Ind. Eng. Chem, 27(12), 1436–1440.

PARKINSON, L., SEDEV, R., FORNASIERO, D., RALSTON, J. 2008. *The terminal rise velocity of 10-100 microm diameter bubbles in water.* J. Colloid Interface Sci, 322(1), 168–172.

PFISTER, M., HAGER, W. H. 2014. *History and Significance of the Morton Number in Hydraulic Engineering.* Journal of Hydraulic Engineering, 140(5), 2514001.

REDFIELD, J. A., HOUGHTON, G. 1965. *Mass transfer and drag coefficients for single bubbles at Reynolds numbers of 0·02–5000.* Chem. Eng. Sci, 20(2), 131–139.

ROSENBERG B. 1950. *The Drag and shape of air bubbles moving in liquids / by Benjamin Rosenberg.* Navy Dept., David W. Taylor Model Basin,.

S. BAZ-RODRÍGUEZ, A. AGUILAR-CORONA, A. SORIA. 2012. *Rising velocity for single bubbles in pure liquids.* Revista Mexicana de Ingeniería Química, 11(2), 269–278.

SANADA, T., SUGIHARA, K., SHIROTA, M., WATANABE, M. 2008. *Motion and drag of a single bubble in super-purified water.* Fluid Dyn. Res, 40(7–8), 534–545.

SCHWERDTFEGER, K. 1968. *Velocity of rise of argon bubbles in mercury.* Chem. Eng. Sci, 23(8), 937–938.

STOKES, G. G. 1851. *ON THE EFFECT OF THE INTERNAL FRICTION OF FLUIDS ON THE MOTION OF PENDULUMS.* Transactions of the Cambridge Philosophical Society, 3, 1880–1905.

STRUMPF, E. 2017. *Experimental study on rise velocities of single bubbles in liquid metal under the influence of strong horizontal magnetic fields in a flat vessel.* Int. J. Multiph. Flow, 97, 168–185.

TADAKI, T., MAEDA, S. 1961. *On the Shape and Velocity of Single Air Bubbles Rising in Various Liquids.* Chemical Engineering, 25(4), 254–264.

TARKAN, H. M., FINCH, J. A. 2005. *Air-assisted solvent extraction: Towards a novel extraction process.* Minerals Engineering, 18(1), 83–88.

TOMIYAMA, A., CELATA, G. P., HOSOKAWA, S., YOSHIDA, S. 2002. *Terminal velocity of single bubbles in surface tension force dominant regime.* International Journal of Multiphase Flow, 28(9), 1497–1519.

TOMIYAMA, A., KATAOKA, I., ZUN, I., SAKAGUCHI, T. 1998. *Drag Coefficients of Single Bubbles under Normal and Micro Gravity Conditions.* JSME International Journal Series B Fluids and Thermal Engineering, 41(2), 472–479.

TSUCHIYA, KATSUM., FAN, L.-SHIH., TSUCHIYA, K. HOWAR. 2013. *Bubble Wake Dynamics in Liquids and Liquid-Solid Suspensions.*

UNO, S., KINTNER, R. C. 1956. *Effect of wall proximity on the rate of rise of single air bubbles in a quiescent liquid.* AIChE J, 2(3), 420–425.

WALLIS, G. B. 1969. *One-dimensional two-phase flow.* New York: McGraw-Hill.

WANG, S., ZHANG, Y., MEREDITH, J. C., BEHRENS, S. H., TRIPATHI, M. K., SAHU, K. C. 2018. *The dynamics of rising oil-coated bubbles: Experiments and simulations.* In Soft Matter (Vol. 14, Number 14, pp. 2724–2734).

WANG, Z. H., WANG, S. D., MENG, X., NI, M. J. 2017. *UDV measurements of single bubble rising in a liquid metal Galinstan with a transverse magnetic field.* Int. J. Multiph. Flow, 94, 201–208.

YAN, X., JIA, Y., WANG, L., CAO, Y. 2017. *Drag coefficient fluctuation prediction of a single bubble rising in water.* Chemical Engineering Journal, 316, 553–562.

YIANATOS, J. B., FINCH, J. A., DOBBY, G. S., XU, M. 1988. *Bubble size estimation in a bubble swarm.* Journal of Colloid and Interface Science, 126(1), 37–44.

ZHANG, C., ECKERT, S., GERBETH, G. 2005. *Experimental study of single bubble motion in a liquid metal column exposed to a DC magnetic field.* Int. J. Multiph. Flow, 31(7), 824–842.